

Testing Yukawa-unified SUSY during year 1 of LHC: the role of multiple b -jets, dileptons and missing E_T

Howard Baer^a, Sabine Kraml^b, Andre Lessa^a and Sezen Sekmen^c

^a*Dept. of Physics and Astronomy, University of Oklahoma, Norman, OK 73019, USA*

^b*Laboratoire de Physique Subatomique et de Cosmologie, UJF Grenoble 1, CNRS/IN2P3, INPG, 53 Avenue des Martyrs, F-38026 Grenoble, France*

^c*Dept. of Physics, Florida State University, Tallahassee, FL 32306*

E-mail: baer@nhn.ou.edu, sabine.kraml@lpsc.in2p3.fr, lessa@nhn.ou.edu, sezen.sekmen@cern.ch

ABSTRACT: We examine the prospects for testing SO(10) Yukawa-unified supersymmetric models during the first year of LHC running at $\sqrt{s} = 7$ TeV, assuming integrated luminosity values of $\sim 0.1\text{--}1$ fb⁻¹. We consider two cases: the Higgs splitting (HS) and the D -term splitting (DR3) models. Each generically predicts light gluinos and heavy squarks, with an inverted scalar mass hierarchy. We hence expect large rates for gluino pair production followed by decays to final states with large b -jet multiplicity. For 0.2 fb⁻¹ of integrated luminosity, we find a 5σ discovery reach of $m_{\tilde{g}} \sim 400$ GeV even if missing transverse energy, E_T^{miss} , is not a viable cut variable, by examining the multi- b -jet final state. A corroborating signal should stand out in the opposite-sign (OS) dimuon channel in the case of the HS model; the DR3 model will require higher integrated luminosity to yield a signal in the OS dimuon channel. This region may also be probed by the Tevatron with $5\text{--}10$ fb⁻¹ of data, if a corresponding search in the multi- $b + E_T^{\text{miss}}$ channel is performed. With higher integrated luminosities of ~ 1 fb⁻¹, using E_T^{miss} plus a large multiplicity of b -jets, LHC should be able to discover Yukawa-unified SUSY with $m_{\tilde{g}} \lesssim 630$ GeV. Thus, the year 1 LHC reach for Yukawa-unified SUSY should be enough to either claim a discovery of the gluino, or to very nearly rule out this class of models, since higher values of $m_{\tilde{g}}$ lead to rather poor Yukawa unification.

KEYWORDS: Supersymmetry Phenomenology, Supersymmetric Standard Model, Large Hadron Collider.

1. Introduction

Grand unified theories (GUTs) find a welcome inclusion of supersymmetry (SUSY) into their structure in that SUSY tames the gauge hierarchy problem via the well-known cancellation of quadratic divergences [1]. In particular, the GUT group $SO(10)$ is highly motivated in that it allows for– in addition to gauge unification– the unification of all the matter superfields of each generation into the 16-dimensional spinor representation [2]. The matter unification only works if the 15 matter superfields of the Minimal Supersymmetric Standard Model (MSSM) are augmented by a SM gauge singlet superfield \hat{N}_i^c which contains a right-hand neutrino (RHN) field. The presence of RHN fields is essential to describe data from the past decade on neutrino mass and flavor oscillations; in particular a Majorana mass term near the GUT scale, needed to implement see-saw neutrino masses [3], should be generated by the breakdown of $SO(10)$ gauge symmetry. In addition to gauge and matter unification, in the simplest $SO(10)$ SUSY GUT models– wherein both MSSM Higgs doublets reside in a 10 of $SO(10)$ – one expects *Yukawa coupling unification* in the third generation: $f_t = f_b = f_\tau$ ($= f_{\nu_\tau}$) at M_{GUT} .

Recently, a variety of studies have examined the MSSM(+RHN) to check whether the measured values of gauge couplings and third generation fermion masses do indeed allow for $t - b - \tau$ Yukawa coupling unification [4–15]. Essential to the calculation is the inclusion of 2-loop renormalization group equations [16] (RGEs) and inclusion of weak scale threshold corrections [17] which occur due to the MSSM \rightarrow SM transition in effective field theories. These threshold corrections imply that Yukawa coupling unification depends on the entire spectrum of SUSY particles, since the SUSY particles enter the various t , b and τ self-energy diagrams [17].

Assuming universal boundary conditions at the GUT scale, the parameter space of $SO(10)$ -motivated SUSY consists of

$$m_{1/2}, m_{16}, m_{10}, M_D^2, A_0, \tan \beta, \text{sign}(\mu), \quad (1.1)$$

where $m_{1/2}$ is the common gaugino mass at M_{GUT} , m_{16} is the common GUT mass of all matter scalars, m_{10} is that of the Higgs soft terms, and M_D^2 parametrizes potential splittings in the GUT scale Higgs (and possibly matter scalar) soft terms. Such splittings are expected to arise from the breaking of the $SO(10)$. It has been found that $t - b - \tau$ Yukawa coupling unification can occur in the MSSM within this setup, but only for very restricted forms of the soft SUSY breaking (SSB) parameters at M_{GUT} . These include, for the case of $\mu > 0$:

- $A_0^2 = 2m_{10}^2 = 4m_{16}^2$,
- $m_{16} \sim 5 - 15 \text{ TeV}$,
- $m_{1/2} \ll m_{16}$,
- $\tan \beta \sim 50$.

These boundary conditions were found in Ref. [18] to give rise to an inverted scalar mass hierarchy (IMH), wherein first/second generation scalars end up with masses ~ 10 TeV, while third generation scalars, Higgs scalars A , H and H^\pm and μ are of order $\sim 1 - 2$ TeV.

A problem with the IMH scheme is that it is inconsistent with radiative electroweak symmetry breaking (REWSB), unless the Higgs soft terms are split at M_{GUT} [19]: $m_{H_u}^2 < m_{H_d}^2$, thus giving $m_{H_u}^2$ a head start over $m_{H_d}^2$ in its running towards the weak scale.¹ Such splitting naturally occurs due to D -term (DT) contributions to *all* scalar masses arising from the breakdown of $SO(10)$. However, applying the splitting to *only* the Higgs sector (“just-so” Higgs splitting, HS)

$$m_{H_{u,d}}^2 = m_{10}^2 \mp 2M_D^2 \quad (\text{HS model}) \quad (1.2)$$

results in better accuracy of Yukawa unification as compared to full DT splitting. Recently, it has been shown that DT splitting, combined with the running effect of the neutrino Yukawa coupling $f_{\nu\tau}$ and a small mass splitting between first/second versus third generation scalars (the DR3 model) can allow for Yukawa coupling unification to a few percent [15].

Both the HS and DR3 schemes lead to sparticle mass spectra characterized by

- $m_{\tilde{q},\tilde{\ell}}(1,2) \sim 10$ TeV,
- $m_{\tilde{q},\tilde{\ell}}(3)$ and $\mu \sim 1 - 3$ TeV,
- $m_{\tilde{g}} \sim 300 - 500$ GeV,
- $m_{\tilde{W}_1,\tilde{Z}_2} \sim 100 - 180$ GeV,
- $m_{\tilde{Z}_1} \sim 50 - 90$ GeV.

Figure 1 shows the location of a large number of Yukawa-unified models in the R vs. $m_{\tilde{g}}$ plane, for the HS model (red dots) and the DR3 model (blue dots) obtained through a Markov Chain Monte Carlo (MCMC) scan of the parameter space (for details, see [15]). Here, the degree of Yukawa unification is quantified as

$$R = \frac{\max(f_t, f_b, f_\tau)}{\min(f_t, f_b, f_\tau)} \quad (1.3)$$

where f_t , f_b and f_τ are the top, bottom and tau Yukawa couplings, respectively, evaluated at $Q = M_{\text{GUT}}$. In the DR3 case, if we require $R < 1.05$, then $m_{\tilde{g}} \lesssim 450$ GeV. In the HS model, while $m_{\tilde{g}} \sim 300 - 500$ GeV is favored for low $R < 1.05$ solutions, it is possible (but not likely) to have occasional models with $m_{\tilde{g}}$ as large as ~ 700 GeV.

In models with the above listed superpartner spectrum and a bino-like \tilde{Z}_1 state, the neutralino relic density is computed to be $\sim 10^2 - 10^4$ times the measured abundance [9,11], and the models are seemingly excluded. However, if one invokes the Peccei-Quinn solution to the strong CP problem [20–24], then an axion/axino supermultiplet is expected in the theory [25]. With an axino of mass $m_{\tilde{a}} \sim 1$ MeV the neutralinos will decay via $\tilde{Z}_1 \rightarrow \tilde{a}\gamma$,

¹This can be different in non-universal models, see [10,13,14].

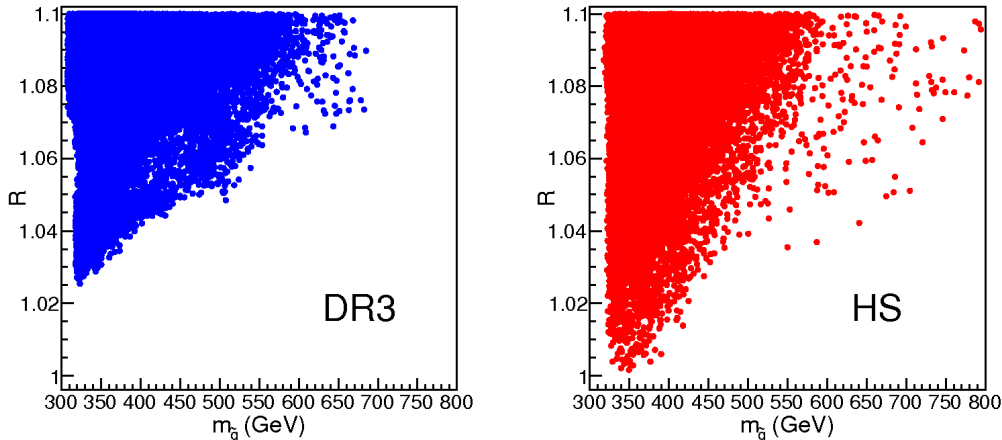


Figure 1: Scatter plot of Yukawa unified models in the R vs. $m_{\tilde{g}}$ plane, for solutions in the DR3 model (blue) and the HS model (red).

which greatly reduces the dark matter density by a large factor: $m_{\tilde{a}}/m_{\tilde{Z}_1}$. Cold dark matter (CDM) solutions can be found consisting of mainly cold axions and thermally produced axinos, with a small component of warm axinos arising from $\tilde{Z}_1 \rightarrow \gamma \tilde{a}$ decay, which occurs on time scales of order 1 sec. Since $m_{16} \sim 10$ TeV, and we expect $m_{16} \sim m_{\tilde{G}}$, the axion/axino CDM scenario allows for a solution to the gravitino BBN problem, and can generate re-heat temperatures $T_R \sim 10^6 - 10^9$ GeV, which can allow for baryogenesis mechanisms such as non-thermal [26] or Affleck-Dine [27] leptogenesis to occur [28].

Since the value of $m_{\tilde{g}}$ is so low in Yukawa-unified SUSY models, we expect the whole scenario to soon be tested at the CERN LHC.² LHC has already turned on in Fall, 2009. As time progresses, the centre-of-mass energy \sqrt{s} will be increased into the ~ 7 TeV regime. An integrated luminosity of $0.1 - 1$ fb⁻¹ is expected to be collected.³ Earlier work on Yukawa-unified SUSY at LHC with $\sqrt{s} = 14$ TeV showed the model to be easily testable at LHC [30]. The LHC SUSY events should be characterized by gluino pair production followed by three-body decays to states including a high multiplicity of b -jets. In addition, opposite-sign dileptons with mass between $40 - 80$ GeV (*i.e.* between the γ and Z peaks) may be evident.

In the intervening past year, while LHC recovered from an unfortunate incident involving faulty circuits and quenched magnets, the experiments have been measuring millions of cosmic muon events. This cosmic data has allowed them to fine-tune their detector response to muons, and to make great strides in alignment of detector elements. We expect thus that isolated muons, jets and b -jets should be readily measurable very early on during LHC running, while reliable electron identification (e ID) and even more so reliable E_T^{miss} measurement, may require additional time to establish.

²Indeed experiments at the Fermilab Tevatron collider may also probe up to $m_{\tilde{g}} \sim 400 - 430$ GeV [29].

³The quoted physics data to be collected at 7 TeV as of November 2009 is 0.2 fb⁻¹.

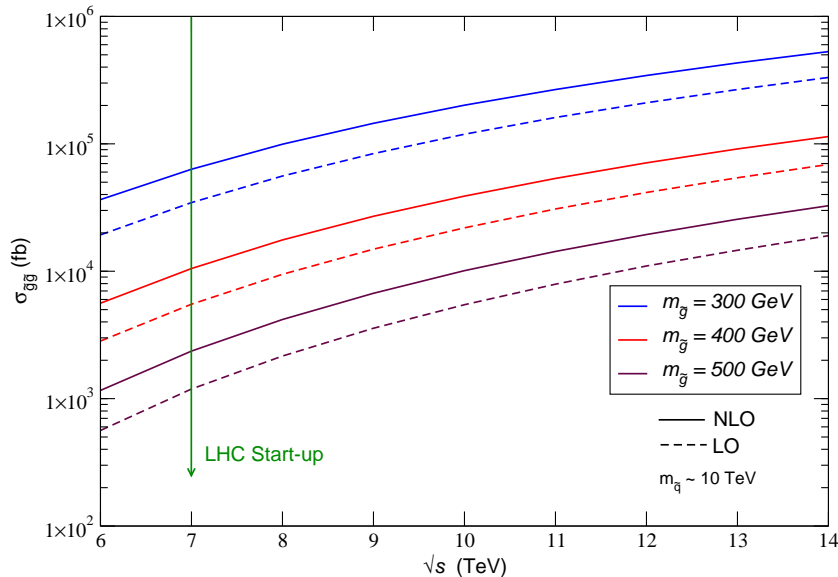


Figure 2: Total cross-section for gluino pair production with $m_{\tilde{q}} = 10$ TeV versus LHC collider energy \sqrt{s} , for $m_{\tilde{g}} = 300, 400$ and 500 GeV.

In this paper, we expand upon the analysis presented in Ref. [30], and address several new issues:

- We focus on the LHC potential to discover or rule out Yukawa-unified SUSY during year 1 of running.⁴ To this end, we calculate signal and background production rates for the LHC turn-on energy of $\sqrt{s} = 7$ TeV rather than the maximal collider energy of $\sqrt{s} = 14$ TeV used earlier. Part of the effect of LHC turn-on at lower than expected energies can be gleaned from Fig. 2, where we plot $\sigma(pp \rightarrow \tilde{g}\tilde{g}X)$ vs. collider energy \sqrt{s} , for $m_{\tilde{g}} = 300, 400$ and 500 GeV, while taking $m_{\tilde{q}} = 10$ TeV. We show both LO and NLO QCD results as derived from Prospino [34]. For $m_{\tilde{g}} = 400$ GeV, LHC operating at $\sqrt{s} = 7$ TeV yields a cross section of $\sigma \sim 10^4$ fb. It is expected that, after about 0.1 fb^{-1} of integrated luminosity, the LHC will move up in energy to the $\sqrt{s} \sim 10$ TeV regime, where $\sigma \sim 3 \times 10^4$ fb. Ultimately, the LHC should move up to its design energy of $\sqrt{s} = 14$ TeV, where the cross section increases to $\sim 10^5$ fb. Various background rates will also change accordingly. In this paper, we take a conservative approach, and evaluate all signal and background cross sections at $\sqrt{s} = 7$ TeV. Increasing the beam energy beyond 7 TeV should only increase the SUSY reach projections which we calculate here.
- We include as well many more background subprocesses than before, including the effect of many $2 \rightarrow 3$ and $2 \rightarrow 4$ body subprocesses.
- We particularly hone in on what LHC can accomplish with very low integrated luminosity. After turn-on, some time will be required to examine detector response to

⁴Some additional analyses of early physics prospects at LHC are contained in Refs. [31–33].

well-known SM processes like W , Z and $t\bar{t}$ production. To be able to use the classic SUSY signature of $jets + E_T^{\text{miss}}$ production, the measurement of E_T^{miss} — which depends on a knowledge of the entire detector response— will be required. However, in Ref. [32,33], it is pointed out that LHC experiments can examine multi-jet + isolated multi-muon events in lieu of $jets + E_T^{\text{miss}}$ events as a gain for signal over background. We find that for very low integrated luminosity, using either large isolated muon multiplicity, or large b -jet multiplicity, allows $m_{\tilde{g}}$ values of up to 400 GeV to be probed with just 0.2 fb^{-1} of integrated luminosity. (Note that we expect a similar reach for the Tevatron in the $\geq 2 - 3$ b -jets + E_T^{miss} channel with $5 - 10 \text{ fb}^{-1}$ [29].)

- We also discuss the case when E_T^{miss} measurements and e ID are established. Here we find that LHC can explore $m_{\tilde{g}}$ values as high as ~ 630 GeV with 1 fb^{-1} of integrated luminosity. Thus, during year 1 the LHC may well be able to either discover or very nearly rule out Yukawa-unified SUSY.

The paper is organized as follows. We first establish in Sec. 2 two Yukawa-unified model lines: one in the HS model and one in the DR3 model. We also examine general features in sparticle production and decay for these model lines. In Sec. 3, we present some technical details of our signal and background calculations. In Sec. 4, we present expectations for *early* SUSY searches in the multi b -jets channel⁵ *without* using E_T^{miss} cuts. We also examine rates for early multi-muon production plus jets without using E_T^{miss} . We find that the HS and DR3 models may be distinguishable by measuring the ratio of OS dilepton events to multi b -jet events, since both models produce multi- b -jets at a similar rate. However, while OS dimuons from \tilde{Z}_2 decay are abundant in the HS model, they are relatively scarce in the DR3 model. In Sec. 5.4, we move beyond the 0.1 fb^{-1} level, and calculate the LHC reach for the two model lines using as well E_T^{miss} and e ID for 1 fb^{-1} of integrated luminosity. In this case, the 5σ LHC reach should extend to $m_{\tilde{g}} \sim 630$ GeV, enough to cover the bulk of parameter space of these simple Yukawa-unified models. In Sec. 7, we present our conclusions.

2. HS and DR3 model lines

2.1 Model lines

Using the parameter space in Eq. 1.1, Ref. [28] found a large number of SUSY spectral solutions with good Yukawa coupling unification in the HS model. We adopt Point B with $R = 1.02$ of this paper as a Yukawa-unified benchmark point, and label it as HSb. The HSb input parameters and mass spectra are listed in Table 1.

To construct a HS model line, we keep most of the above parameters fixed, but allow $m_{1/2}$ to vary. This keeps the Yukawa-unification generally low, but allows us to vary $m_{\tilde{g}} \sim 3.5m_{\tilde{Z}_2} \sim 7m_{\tilde{Z}_1}$ continuously. We plot the value of R versus $m_{\tilde{g}}$ in Fig. 3. We see that at low $m_{\tilde{g}}$ (~ 325 GeV), $R < 1.03$, while as $m_{\tilde{g}}$ increases, Yukawa unification gets worse until $m_{\tilde{g}} \sim 700$ GeV, where we find $R \sim 1.13$.

⁵Earlier work emphasizing the utility of the presence of b -jets in SUSY events was provided in Refs. [30, 35].

parameter	HSb	DR3b
$m_{16}(1, 2)$	10000	11805.6
$m_{16}(3)$	10000	10840.1
m_{10}	12053.5	13903.3
M_D	3287.1	1850.6
$m_{1/2}$	43.9442	27.414
A_0	-19947.3	-22786.2
$\tan \beta$	50.398	50.002
R	1.025	1.027
μ	3132.6	2183.4
$m_{\tilde{g}}$	351.2	321.4
$m_{\tilde{u}_L}$	9972.1	11914.2
$m_{\tilde{t}_1}$	2756.5	2421.6
$m_{\tilde{b}_1}$	3377.1	1359.5
$m_{\tilde{e}_R}$	10094.7	11968.5
$m_{\tilde{W}_1}$	116.4	114.5
$m_{\tilde{Z}_2}$	113.8	114.2
$m_{\tilde{Z}_1}$	49.2	46.5
m_A	1825.9	668.3
m_h	127.8	128.6

Table 1: Masses in GeV units and parameters for Yukawa-unified benchmark points HSb [28] and DR3b [15]. For the DR3 model, we use $M_{N_3} = 10^{13}$ GeV.

We also adopt from Ref. [15] a DR3 model line, labelled as DR3b, with parameters in Table 1. where $m_{16}(1, 2, 3)$, is the scalar mass for the 1st, 2nd and 3th generations and M_{N_3} , $f_{\nu\tau}$, $A_{\nu\tau}$ and $m_{\tilde{\nu}_{R3}}$ are the right-handed neutrino mass, Yukawa coupling, A -term and the scalar mass for the sneutrino. We construct a DR3 model line by again keeping most parameters fixed, but letting $m_{1/2}$ to vary. In the DR3 model line, we find $R \sim 1.03$ for $m_{\tilde{g}} \sim 325$ GeV, while R increases to ~ 1.15 for $m_{\tilde{g}} \sim 700$ GeV.⁶

Due to the heavy scalar masses in the HS and DR3 model lines, the scalars essentially decouple at LHC energies. What results is a low energy effective theory where only \tilde{g} , $\tilde{Z}_{1,2}$ and \tilde{W}_1^\pm are the new physics matter states. In the next two sections we discuss the production cross-sections and decay rates for these states.

2.2 HS and DR3 production cross sections

We plot in Fig. 4 the leading order $\tilde{g}\tilde{g}$, $\tilde{W}_1\tilde{Z}_2$ and $\tilde{W}_1^+\tilde{W}_1^-$ production cross sections as a function of $m_{\tilde{g}}$ for collider energy $\sqrt{s} = 7$ TeV. From the figure, we see that gluino pair production is dominant up to $m_{\tilde{g}} \sim 520$ GeV (at NLO, it dominates up to $m_{\tilde{g}} \sim 560$ GeV), with cross sections typically greater than 10^3 fb, and in excess of 10^4 fb in the lower gluino mass range. Thus, even with integrated luminosities as low as 0.1 fb^{-1} , we expect hundreds

⁶Although Fig. 1 shows that for some special choice of the parameters lower values of R can be obtained for $m_{\tilde{g}} \sim 700$, the model lines chosen here represent the general behavior of the bulk of parameter space.

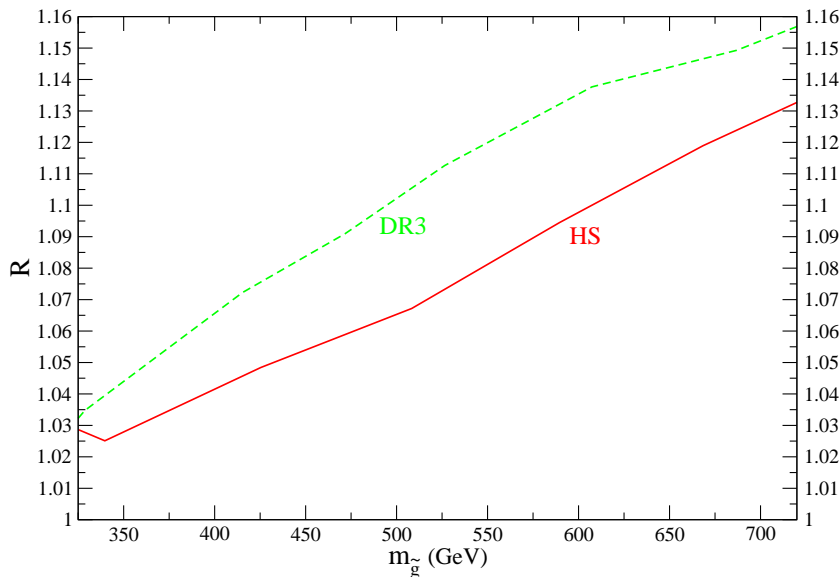


Figure 3: Degree of Yukawa unification R (see Eq.1.3) for the models HS and DR3 as a function of the gluino mass. The model parameters are the same as in Table 1, but with $m_{1/2}$ varying from 30 to 180 GeV.

of gluino pair events in the upcoming LHC year 1 physics data sample for the HS and DR3 models.

Gluino pair production cross sections at the Fermilab Tevatron collider show a large increase in rate as $m_{\tilde{g}}$ increases [29]. This is due to suppression of negative interference terms in the $q\bar{q} \rightarrow \tilde{g}\tilde{g}$ subprocess cross section. At the LHC, gluino pair production for $m_{\tilde{g}} \sim 300-500$ GeV is dominated instead by the $gg \rightarrow \tilde{g}\tilde{g}$ subprocess, which is independent of $m_{\tilde{g}}$. Thus, $\tilde{g}\tilde{g}$ cross sections show only a slight ($\sim 10-20\%$) increase with increasing $m_{\tilde{g}}$ at the LHC.

2.3 Sparticle branching fractions in the HS and DR3 model lines

Since $m_{\tilde{g}} \ll m_{\tilde{q}}$ in the HS or DR3 model lines, we will get dominant gluino decays into three-body modes. The gluino branching ratios will be largely model dependent, but since \tilde{t}_i and \tilde{b}_i are always the lightest squarks, and $\tan\beta$ is large [36], the decays will mostly be restricted to the following channels:

- $\tilde{g} \rightarrow \tilde{Z}_i + b\bar{b}$, $i = 1, 2$
- $\tilde{g} \rightarrow \tilde{Z}_1 + t\bar{t}$
- $\tilde{g} \rightarrow \tilde{W}_1^- b\bar{t}$ or $\tilde{W}_1^+ b\bar{t}$.

The general feature $m_{\tilde{g}} \ll m_{\tilde{q}}$ is common to both the HS and DR3 models, since it relies mostly on the fact that $m_{1/2} \ll m_{16}$. However, the inclusion of the D -term splitting

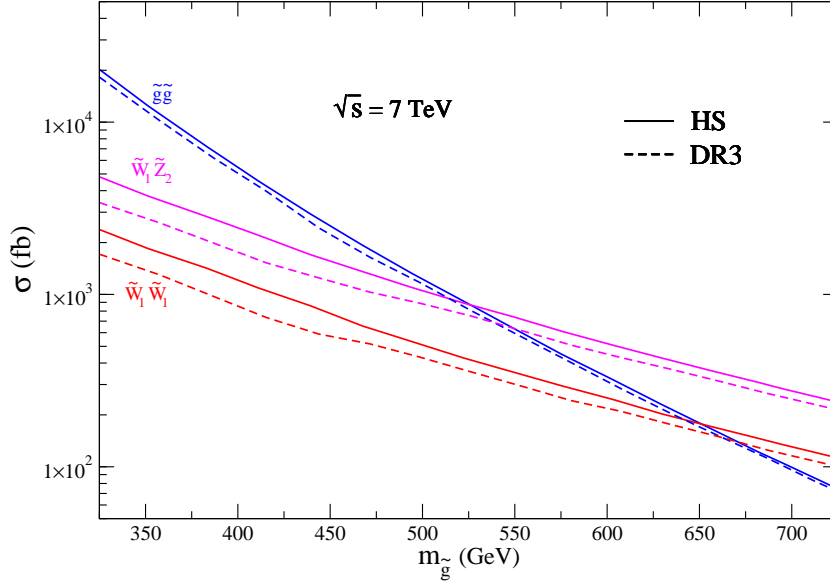


Figure 4: Leading order total cross-sections for sparticle production in the HS model (solid) and DR3 model (dashed) as a function of the gluino mass for pp collisions at $\sqrt{s} = 7$ TeV. The model parameters are the same as in Table 1 but with $m_{1/2}$ varying from 30 to 180 GeV.

for all matter scalars in the DR3 model pushes $m_{\tilde{b}_R}$ to lower values, when compared to the HS model, where $m_{\tilde{b}_L} \sim m_{\tilde{b}_R}$.⁷ As a result we have:

- DR3: $\tilde{b}_1 \sim \tilde{b}_R$ and $m_{\tilde{b}_1} < m_{\tilde{b}_2}$
- HS: $\tilde{b}_1 \sim \tilde{b}_L$ and $m_{\tilde{b}_1} \sim m_{\tilde{b}_2}$

Now, since \tilde{Z}_2 is wino-like in both models, it just couples to left-squarks, what suppresses the $\tilde{g} \rightarrow \tilde{Z}_2 + b\bar{b}$ decay in the DR3 model and favors it in the HS case. This behavior is shown in Fig. 5, where the main gluino branching ratios for both models are plotted as a function of the gluino mass. From Fig. 5 it can also be seen that— in the HS model— once $m_{\tilde{g}} \gg m_t + m_{\tilde{W}_1}$ the $\tilde{g} \rightarrow \tilde{W}_1^- b t + c.c.$ channel starts to dominate, since $m_{\tilde{t}_1} < m_{\tilde{b}_1}$ (for $m_{\tilde{g}} > 500$ GeV). We can also see that $\tilde{g} \rightarrow \tilde{Z}_1 t \bar{t}$ becomes relevant for heavy gluinos ($m_{\tilde{g}} > 600$ GeV) and it is enhanced in the DR3 model, where \tilde{t}_1 is usually lighter than in the HS model.

From Fig. 5 we see that, for the HSb benchmark case:

- $BR(\tilde{g} \rightarrow \tilde{Z}_2 + b\bar{b}) = 63\%$
- $BR(\tilde{g} \rightarrow \tilde{Z}_1 + b\bar{b}) = 15\%$
- $BR(\tilde{g} \rightarrow \tilde{W}_1 + bt) = 9\%$.

On the other hand, the DR3b point has:

⁷The stop masses and mixing are basically the same in both models, since the D -term splitting is equal for both \tilde{t}_R and \tilde{t}_L .

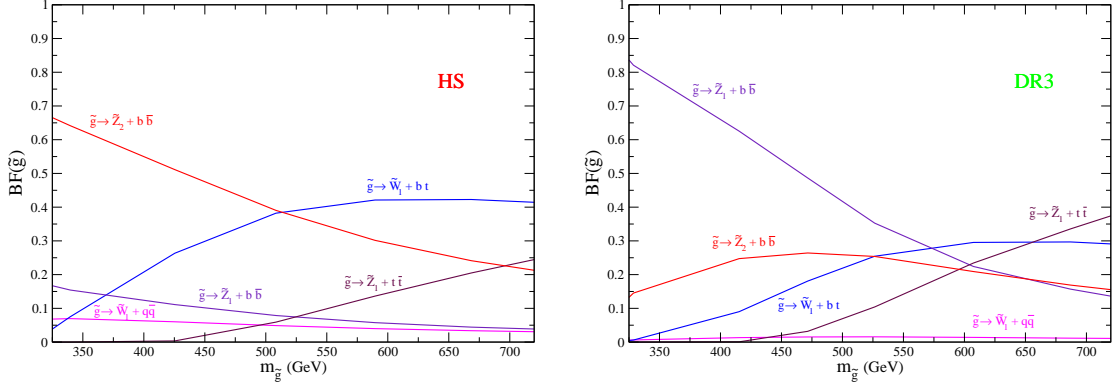


Figure 5: Gluino branching ratios for the HS and DR3 model-lines as a function of the gluino mass. The model parameters are the same as in Table 1, but with $m_{1/2}$ varying from 30 to 180 GeV.

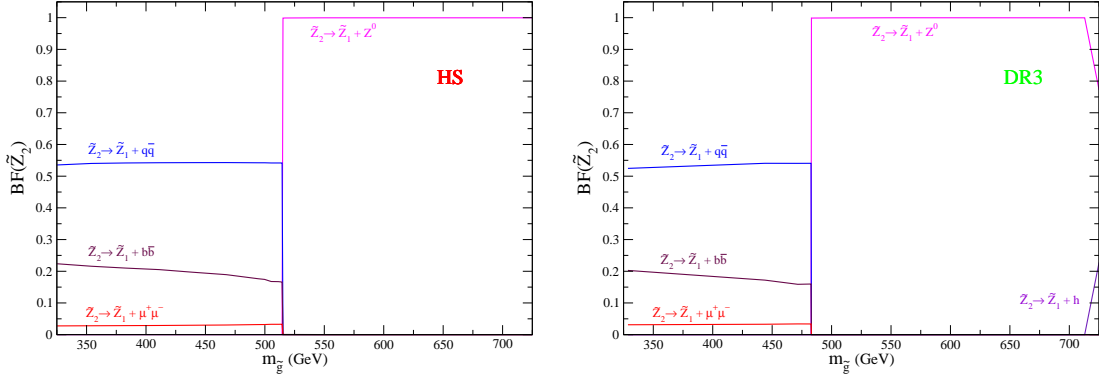


Figure 6: \tilde{Z}_2 branching ratios for the HS and DR3 model-lines as a function of the gluino mass. The model parameters are the same as in Table 1, but with $m_{1/2}$ varying from 30 to 180 GeV.

- $BR(\tilde{g} \rightarrow \tilde{Z}_2 + b\bar{b}) = 11\%$
- $BR(\tilde{g} \rightarrow \tilde{Z}_1 + b\bar{b}) = 86\%$
- $BR(\tilde{g} \rightarrow \tilde{W}_1 + bt) = 0.3\%$.

The \tilde{Z}_2 and \tilde{W}_1 are expected to decay via three body modes:

- $\tilde{Z}_2 \rightarrow \tilde{Z}_1 f \bar{f}$
- $\tilde{W}_1^\pm \rightarrow \tilde{Z}_1 f \bar{f}'$,

where the decays are dominated by the intermediate virtual W^* and Z^* diagrams. If $m_{\tilde{g}} \gtrsim 500$ GeV, then the two-body modes $\tilde{W}_1 \rightarrow \tilde{Z}_1 W$ and $\tilde{Z}_2 \rightarrow \tilde{Z}_1 Z$ will turn on.

Putting all segments of the cascade decays together, we expect the HSb signal to be rich in b -jets and opposite-sign/same-flavor (OS/SF) isolated dileptons coming from $\tilde{Z}_2 \rightarrow \tilde{Z}_1 \ell \bar{\ell}$, with a small rate of SS dileptons coming from $\tilde{g} \rightarrow \tilde{W}_1 q \bar{q}'$ followed by $\tilde{W}_1 \rightarrow \ell \nu_\ell \tilde{Z}_1$ decay. For the DR3b point, we expect the signal to be rich in b -jets with a harder E_T^{miss} spectrum

SM process	Generator	Cross section	number of events
QCD: 2, 3 and 4 jets ($p_T > 40$ GeV)	AlpGen	3.0×10^9 fb	13M
$t\bar{t}$: $t\bar{t} + 0, 1$ and 2 jets	AlpGen	1.6×10^5 fb	5M
$b\bar{b}$: $b\bar{b} + 0, 1$ and 2 jets	AlpGen	8.8×10^7 fb	91M
$Z + \text{jets}$: $Z/\gamma(\rightarrow l\bar{l}, \nu\bar{\nu}) + 0, 1, 2$ and 3 jets	AlpGen	8.8×10^6 fb	13M
$W + \text{jets}$: $W^\pm(\rightarrow l\nu) + 0, 1, 2$ and 3 jets	AlpGen	1.8×10^7 fb	19M
$Z + t\bar{t}$: $Z/\gamma(\rightarrow l\bar{l}, \nu\bar{\nu}) + t\bar{t} + 0, 1$ and 2 jets	AlpGen	53 fb	0.6M
$Z + b\bar{b}$: $Z/\gamma(\rightarrow l\bar{l}, \nu\bar{\nu}) + b\bar{b} + 0, 1$ and 2 jets	AlpGen	2.6×10^3 fb	0.3M
$W + b\bar{b}$: $W^\pm(\rightarrow l\nu) + b\bar{b} + 0, 1$ and 2 jets	AlpGen	6.4×10^3 fb	9M
$t\bar{t}t\bar{t}$	MadGraph	0.6 fb	1M
$t\bar{t}b\bar{b}$	MadGraph	1.0×10^2 fb	0.2M
$b\bar{b}b\bar{b}$	MadGraph	1.1×10^4 fb	0.07M

Table 2: Background processes included in this study, their cross sections and number of generated events.

(when compared to HSb) due to the direct gluino decay to \tilde{Z}_1 , but with small rates in the multilepton channels.

3. Event Simulation

In order to study the discovery potential of the LHC at $\sqrt{s} = 7$ TeV we used AlpGen [37] and MadGraph [38] to generate the background hard scattering events and Pythia [39] for the subsequent showering and hadronization. Table 2 lists the $2 \rightarrow n$ subprocesses included in this study where jets = u, d, s, c and g . For all the processes involving multiple jets, the MLM matching algorithm [37] was used to avoid double counting. All the above processes were generated at LO, but a relatively low renormalization and factorization scale ($Q = \sqrt{\hat{s}}/6$) was used to bring the total cross-sections closer to their NLO values (for more details see Ref. [33]). The signal events were generated using Isajet 7.79 [40].

A toy detector simulation is then employed with calorimeter cell size $\Delta\eta \times \Delta\phi = 0.05 \times 0.05$ and $-5 < \eta < 5$. The HCAL (hadronic calorimetry) energy resolution is taken to be $80\%/\sqrt{E} + 3\%$ for $|\eta| < 2.6$ and FCAL (forward calorimetry) is $100\%/\sqrt{E} + 5\%$ for $|\eta| > 2.6$, where the two terms are combined in quadrature. The ECAL (electromagnetic calorimetry) energy resolution is assumed to be $3\%/\sqrt{E} + 0.5\%$. We use the Isajet jet finding algorithm (cone type) to group the hadronic final states into jets. The jets and isolated lepton definitions are as follow:

- Jets are required to have $R \equiv \sqrt{\Delta\eta^2 + \Delta\phi^2} \leq 0.4$ and $E_T(jet) > 25$ GeV.
- Leptons are considered isolated if they have $p_T(l) > 5$ GeV with visible activity within a cone of $\Delta R < 0.2$ of $\Sigma E_T^{cells} < 5$ GeV.

Jets are tagged as b -jets if they contain a B hadron with $E_T(B) > 15$ GeV, $\eta(B) < 3$ and $\Delta R(B, jet) < 0.5$. We assume a tagging efficiency of 60% and light quark and gluon

jets can be mis-tagged as a b -jet with a probability $1/150$ for $E_T \leq 100$ GeV, $1/50$ for $E_T \geq 250$ GeV, with a linear interpolation for $100 \text{ GeV} \leq E_T \leq 250 \text{ GeV}$ (see R. Kadala *et al.* in Ref. [35]).

4. Early searches without E_T^{miss} or electron ID

During the early stages of data taking at the LHC with integrated luminosity of order $\sim 0.1 \text{ fb}^{-1}$, it is possible that E_T^{miss} and electron identification will not be reliable observables (see Refs. [32,33]). Therefore we separate our analysis into two stages:

- early searches, where no E_T^{miss} cuts are applied and only muons are considered for the leptonic channels, and
- full analysis, using a minimum E_T^{miss} cut and including both e 's and μ 's.

In both cases we assume that the b -jets can be reliably tagged due to their displaced vertices as reconstructed in the micro-vertex detector or via a non-isolated muon tag. For initial searches we apply the following set of minimal cuts, labelled C0:

C0 cuts:

- Jet cuts: $n(\text{jets}) \geq 4$ with $E_T(j) \geq 50 \text{ GeV}$, $\eta(j) \leq 3$ and for the hardest jet $E_T(j1) \geq 100 \text{ GeV}$,
- Lepton cuts: $E_T(\ell) \geq 10 \text{ GeV}$ and $\eta(\ell) \leq 2$,
- $S_T \geq 0.2$,
- $n(b) \geq 1$,

where S_T is the transverse sphericity and for now $\ell = \mu$ only.

4.1 Multi b -jet signal

As discussed in Sec. 2 the points HSb and DR3b are expected to be rich in b -jets and possibly isolated leptons. In Fig. 7 we plot the b -jet multiplicity for the signal and backgrounds (BG) after applying the C0 set of cuts. As expected, the BG distribution falls much faster than the signal. Signal exceeds BG for $n(b) \geq 4$, where the BG is dominated by multi b production ($b\bar{b}$ and $b\bar{b}b\bar{b}$). We also note that the DR3b case has larger rates for $1 \leq n(b) \leq 4$ when compared with the HSb point, due to a lighter gluino. However, the HSb benchmark gives a larger signal for $n(b) \geq 5$, since in this case $\tilde{Z}_2 \rightarrow \tilde{Z}_1 b\bar{b}$ also contributes, and \tilde{Z}_2 are produced at large rates from gluino cascade decay.

We note here that a signal rate above an expected SM BG level may not be sufficient to claim a discovery, due to both theoretical and experimental uncertainties in the multi- b background rate. However, the overall *shape* of the $n(b)$ distribution should be to some extent self-normalizing, as one can fix the BG levels in the $n(b) = 0, 1, 2$ channels, and look for a *harder* $n(b)$ distribution in the signal case. Thus, some of the uncertainty is

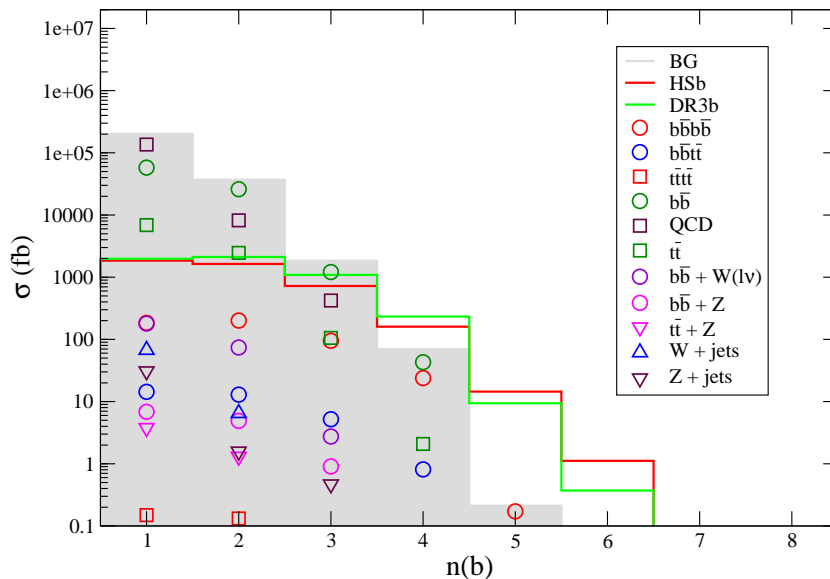


Figure 7: b -jet distribution after C0 cuts at the LHC, with $\sqrt{s} = 7$ TeV. We show the signal levels for the HSb (red) and DR3b (green) points along with various SM backgrounds.

Results after C0-based selection			
	$\sigma(n(b) \geq 3)$	$\sigma(n(b) \geq 4)$	$\sigma(\text{OS})$
HSb	899 fb	176 fb	99 fb
DR3b	1334 fb	243 fb	22 fb
BG	1911 fb	70 fb	11 fb

Table 3: Cross-sections for the $n(b) \geq 3, 4$ and OS channels after the C0 cuts for the points HSb, DR3b and the background.

removed when one looks for an excess in *ratios* such as $\sigma(n(b) = 3)/\sigma(n(b) = 1)$. Table 3 shows the $n(b) \geq 3$ and 4 cross-sections for both points and the background. The signal in the $n(b) \geq 4$ channel is at the 200 fb level and is well above SM background levels. Such a signal may be visible with very low integrated luminosity values $\sim 0.05 \text{ fb}^{-1}$!

As mentioned above, a mere excess in one or more of the multi b -jet channels may not be sufficient to claim discovery, due to large uncertainties in the normalization of the high jet multiplicities BGs, such as $b\bar{b}$, $t\bar{t}$ and $Z + 2$ jets. With this in mind, we present some signal distributions with distinct shapes from the BG ones, which could help corroborate a discovery and provide some information on the sparticle masses. As discussed in Sec. 2, events with $n(b) \geq 4$ usually come from $\tilde{g} \rightarrow \tilde{Z}_i b\bar{b}$ decays. Therefore the invariant mass of the $b\bar{b}$ pair is expected to have edges at $m_{\tilde{g}} - m_{\tilde{Z}_i}$. This is shown in Figs. 8 and 9, where $\max[m_{b_1\bar{b}_1}, m_{b_2\bar{b}_2}]$ is plotted⁸ at the parton level (dashed black line). As expected, in the DR3b case the $m_{\tilde{g}} - m_{\tilde{Z}_1}$ mass edge is much more evident than the $m_{\tilde{g}} - m_{\tilde{Z}_2}$ edge, due to the large $\tilde{g} \rightarrow \tilde{Z}_1 + b\bar{b}$ branching fraction, while the opposite happens for the HSb point. At the detector level, the main difficulty in obtaining $\max[m_{b_1\bar{b}_1}, m_{b_2\bar{b}_2}]$ comes from

⁸Here the index i in b_i labels b 's coming from the same gluino.

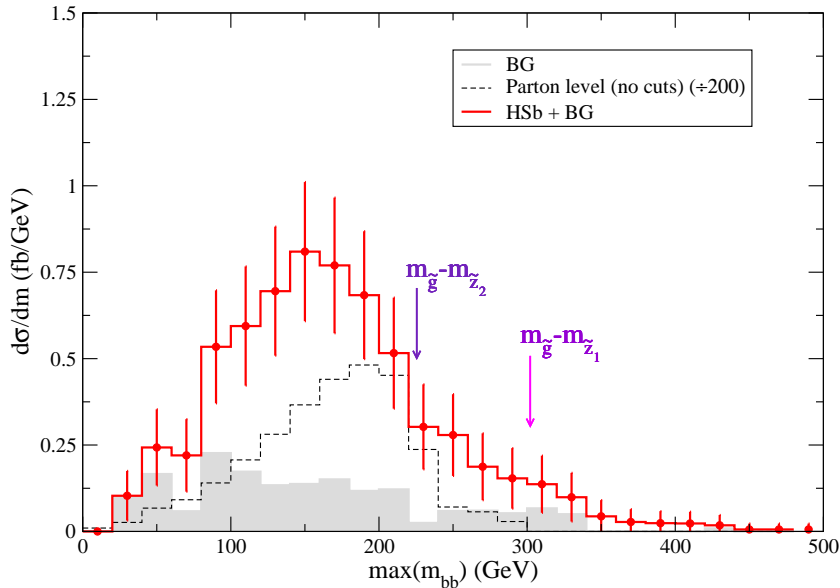


Figure 8: Maximum invariant bb mass at parton level for the HSb point without cuts (black/dashed) and at detector level for the HSb plus background events (red/solid) with $n(b) \geq 4$, $\Delta R(b_2, \bar{b}_2) < 1$ after the C0 cuts (see text). The BG distribution (gray) and the statistical error bars for 1 fb^{-1} of integrated luminosity are also shown.

combining the correct b -jets into pairs coming from the same gluino. As pointed out in Ref. [30], usually the two hardest b -jets come from different gluinos. Furthermore, in most cases the pair coming from the same \tilde{g} has smaller separation angles. Using these two facts, we select b_1 and b_2 as the hardest and second hardest jets and \bar{b}_2 as the remaining jet that minimizes $\Delta\phi(b_2, \bar{b}_2)$. Also, to avoid event topologies with no small angular separation, we apply the cut $\Delta R(b_2, \bar{b}_2) < 1$, where $R = \sqrt{\Delta\phi(b_2, \bar{b}_2)^2 + \Delta\eta(b_2, \bar{b}_2)^2}$. Using this procedure and adding the C0 set of cuts we obtain the solid curves shown in Figs. 8 and 9, where the BG contribution was added to the signal. We also show the statistical error bars for 1 fb^{-1} of integrated luminosity. As can be seen, the invariant-mass distributions have the expected shape, although the mass edges seem to require higher integrated luminosity to become statistically relevant.

4.2 Dimuon channels

In Fig. 10 we show the muon multiplicity for the HSb and DR3b signal points and the BG. For $n(\mu) = 0, 1$, the BG is well above the signal, but for $n(\mu) \geq 2$, signal starts to dominate over the BG. As expected from the discussion in Sec. 2, the DR3b has much smaller rates to multileptons. Separating the $n(\mu) = 2$ channel into opposite sign (OS) and same sign (SS) muons, we see that almost all the signal comes from the OS dimuon case. Due to the small $\tilde{g} \rightarrow \widetilde{W}_1^- t\bar{b} + c.c.$ branching fraction, the SS signal is almost 2 orders of magnitude below the OS one, which makes it irrelevant for luminosities $\lesssim 1 \text{ fb}^{-1}$. As seen in Table 3, the OS cross-section for the HSb point is around 100 fb and has a discovery potential similar to the multi b -jet channel, while the DR3b benchmark will require more

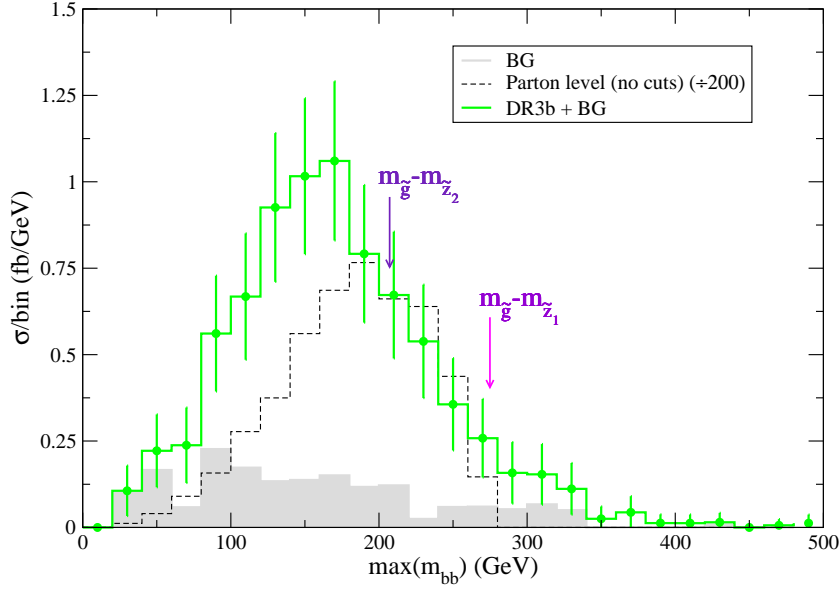


Figure 9: Maximum invariant bb mass at parton level for the DR3b point without cuts (black/dashed) and at detector level for the DR3b plus background events (green/solid) with $n(b) \geq 4$, $\Delta R(b_2, \bar{b}_2) < 1$ after the C0 cuts (see text). The BG distribution (gray) and the statistical error bars for 1 fb^{-1} of integrated luminosity are also shown.

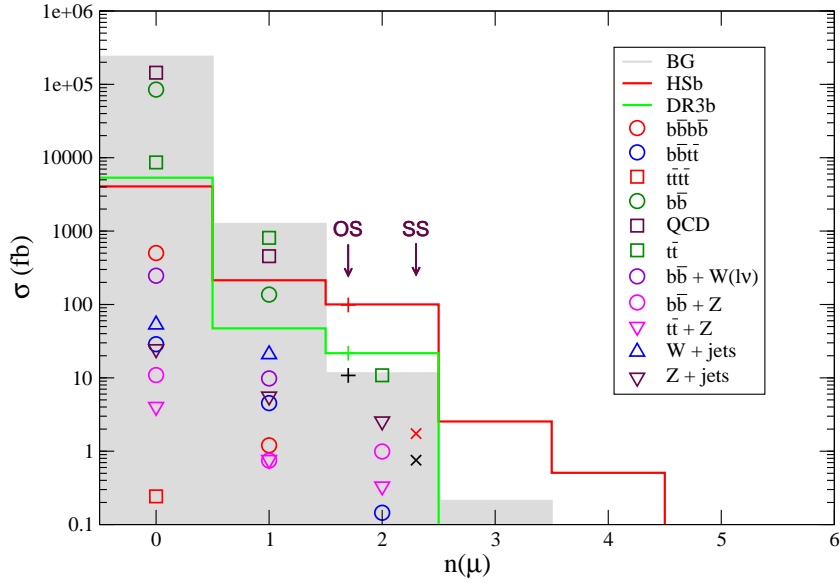


Figure 10: Muon distribution after C0 cuts at the LHC, with $\sqrt{s} = 7 \text{ TeV}$. We show the signal levels for the HSb (red) and DR3b (green) points along with various SM backgrounds. In the $n(\mu) = 2$ bin, the left (pluses) and right (crosses) columns show the background (black) and signal components for OS (with invariant mass cuts) and SS dimuons.

integrated luminosity to be seen in the OS dimuon channel.

As is well known, the invariant mass of OS muons has a mass edge at $m_{\tilde{Z}_2} - m_{\tilde{Z}_1}$, since most OS muons come from $\tilde{Z}_2 \rightarrow \tilde{Z}_1 \mu^+ \mu^-$ decays. In Fig. 11, we show the $m(\mu^+ \mu^-)$

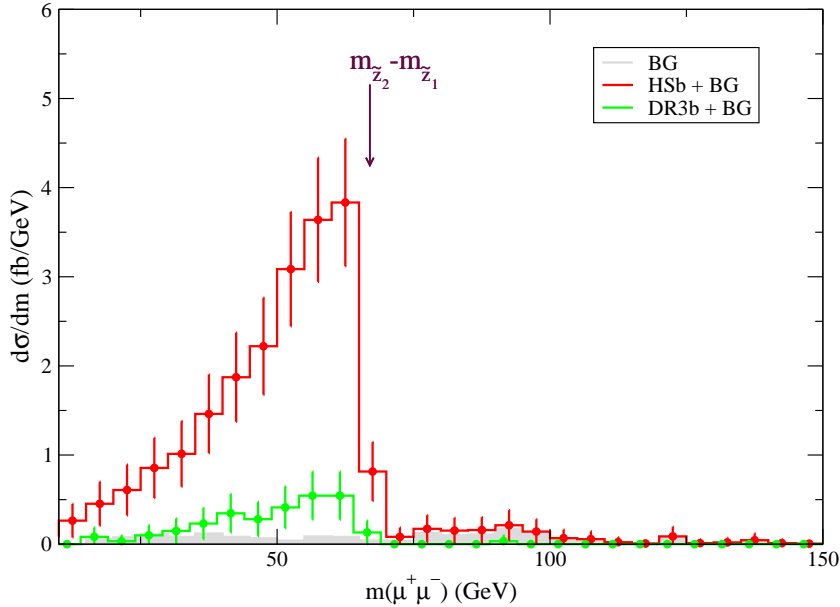


Figure 11: OS dimuon invariant mass for the HSb (red) and DR3b (green) points plus background events after the C0 cuts (see text). The BG distribution (gray) and the statistical error bars for 1 fb^{-1} of integrated luminosity are also shown.

distribution for the HSb and DR3b points. As discussed in Sec. 2, the DR3b point has small leptonic rates but may still be visible above background. In both cases, the mass edges are visible and give the correct $m_{\tilde{Z}_2} - m_{\tilde{Z}_1}$ values. We also show the statistical error bars for the combined signal plus background for 1 fb^{-1} of integrated luminosity. From Fig. 11, we can see that the HSb point gives a statistically significant edge while the DR3b case may require higher integrated luminosities.

Finally, we point out that in both the $n(b) \geq 4$ and OS dimuon channels the invariant mass distributions shown in Figs. 8, 9 and 11 have distinct features from the BG, which should corroborate a discovery claim.

4.3 Early SUSY search: reach results

To estimate the LHC reach in the multi- b and multi- μ channels, we plot in Fig. 12 the signal cross section for the HS and DR3 model lines versus $m_{\tilde{g}}$ using cuts C0 plus $a)$. $n(b) \geq 3$ and $b)$. $n(b) \geq 4$, along with the expected BG rate. We also plot the 5σ discovery lines for integrated luminosity values 0.1 and 0.2 fb^{-1} . The significance in σ s is derived from the p-value corresponding to the number of S+B events in a Poisson distribution with a mean that equals to the number of background events [41]. For both the HS and DR3 model lines, the approximate 5σ LHC reach extends to $m_{\tilde{g}} \sim 360 \text{ GeV}$ for 0.1 fb^{-1} , and $\sim 400 \text{ GeV}$ for 0.2 fb^{-1} . We remind the reader that this is comparable to what Tevatron experiments can achieve using E_T^{miss} cuts and $> 5 \text{ fb}^{-1}$ of integrated luminosity [29].

The reach using cuts C0 and requiring an OS dimuon pair is shown in Fig. 13. In this case, the reach in the HS model is similar to the multi- b reach: LHC should explore to $m_{\tilde{g}} \sim 360 \text{ GeV}$ with 0.1 fb^{-1} , and $m_{\tilde{g}} \sim 400 \text{ GeV}$ with 0.2 fb^{-1} . In the DR3 model

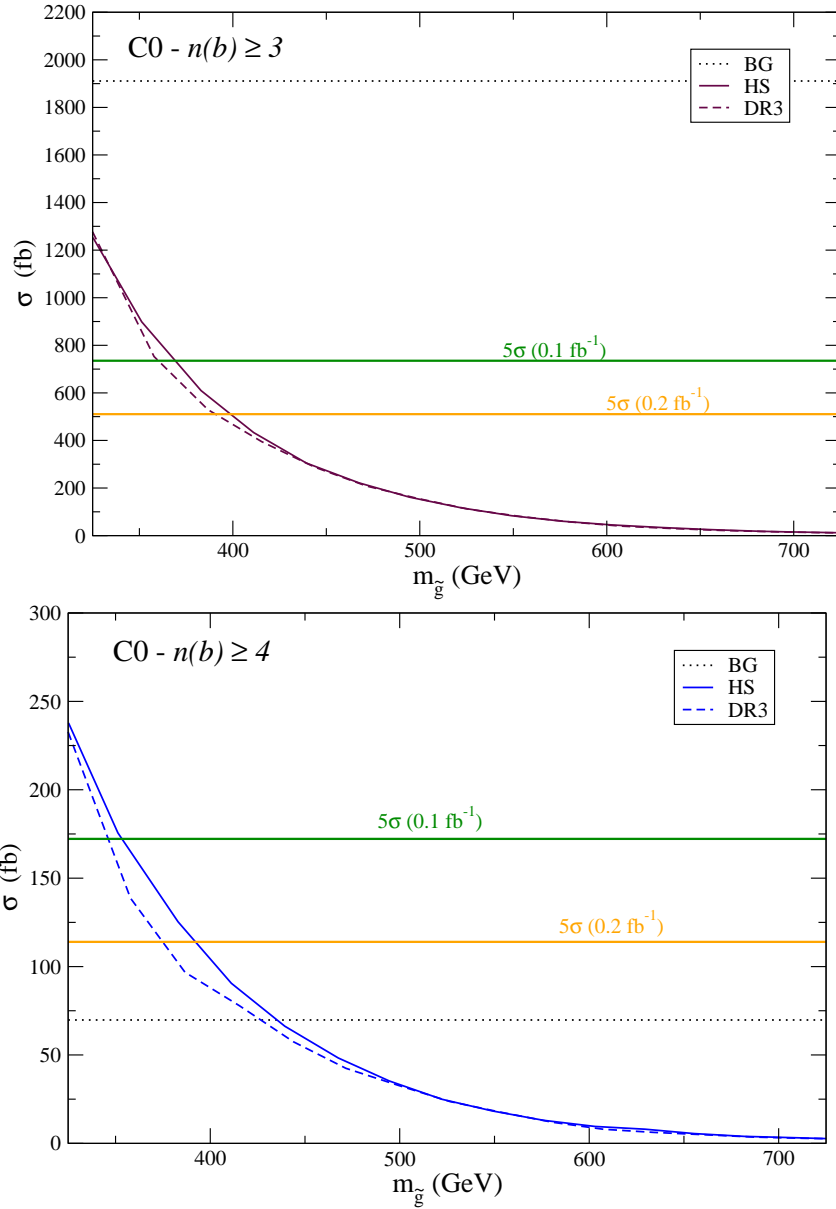


Figure 12: Early LHC reach for Yukawa-unified SUSY using cuts $C0$ plus $n_b \geq 3$ and $n_b \geq 4$.

line, however, there is no reach in the OS dimuon channel at these low values of integrated luminosity. In fact, the rate of multi- b -jet events compared to the rate for OS dimuon events would be one way to distinguish early-on whether one might be seeing SUSY in the HS or the DR3 model case.

We also point out that despite giving the maximum reach for both models, the $n(b) \geq 3$ channel has a small signal/BG ratio, what makes it more dependent on the knowledge of the background.

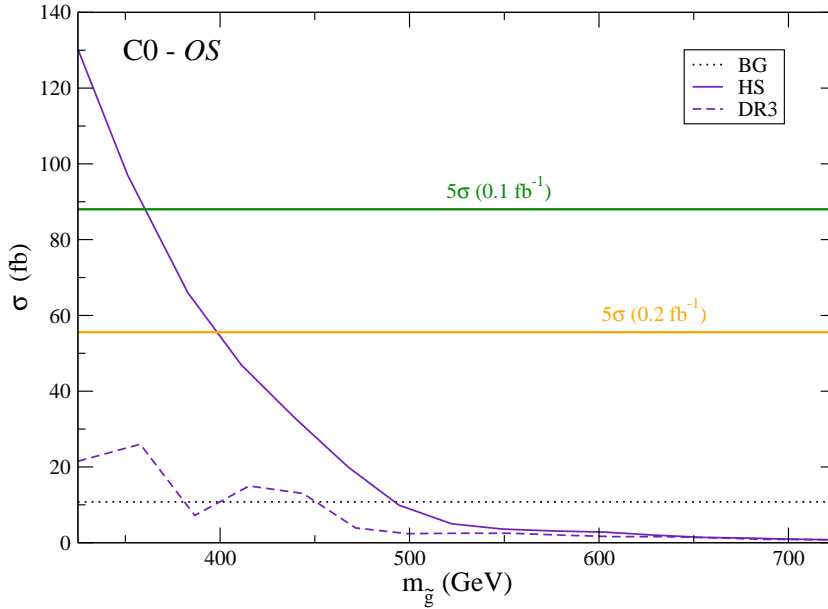


Figure 13: Early LHC reach for Yukawa-unified SUSY using cuts $C0$ plus requiring OS dimuons.

5. Analysis including E_T^{miss} cut and electron ID

As the experiments accumulate data, knowledge of the detectors and their response to SM background will improve. Also, at some point in time, the LHC center-of-mass energy will increase beyond 7 TeV into the 10 TeV range. To be conservative, we will continue our analysis assuming $\sqrt{s} = 7$ TeV. Moving to higher values of \sqrt{s} should only increase the possibility of discovering new, high mass matter states.

As detector response becomes better understood, it will be possible to utilize both E_T^{miss} and electrons in the analysis. The E_T^{miss} variable is well known to be a powerful discriminator between SUSY and SM events, and is considered to be the “classic” signature for SUSY. In Fig. 14 we show the E_T^{miss} distributions for the BG as well as the HSb and DR3b points after applying the $C0$ cuts. As expected, the DR3b signal has a harder E_T^{miss} spectrum than HSb, due to its large $\tilde{g} \rightarrow \tilde{Z}_1 b \bar{b}$ branching ratio.

In order to reduce most of the background and still keep considerably large cross-sections for the signal, we henceforth:

- include the $E_T^{\text{miss}} > 100$ GeV cut and
- include e 's into the $C0$ leptonic cuts

into our analysis. The cuts $C0$ augmented with the E_T^{miss} cut and inclusion of e 's, but with no $n(b)$ requirement, will be called $C1$ cuts:

$C1$ cuts:

- Jet cuts: $n(\text{jets}) \geq 4$ with $E_T(j) \geq 50$ GeV, $\eta(j) \leq 3$ and for the hardest jet $E_T(j1) \geq 100$ GeV,

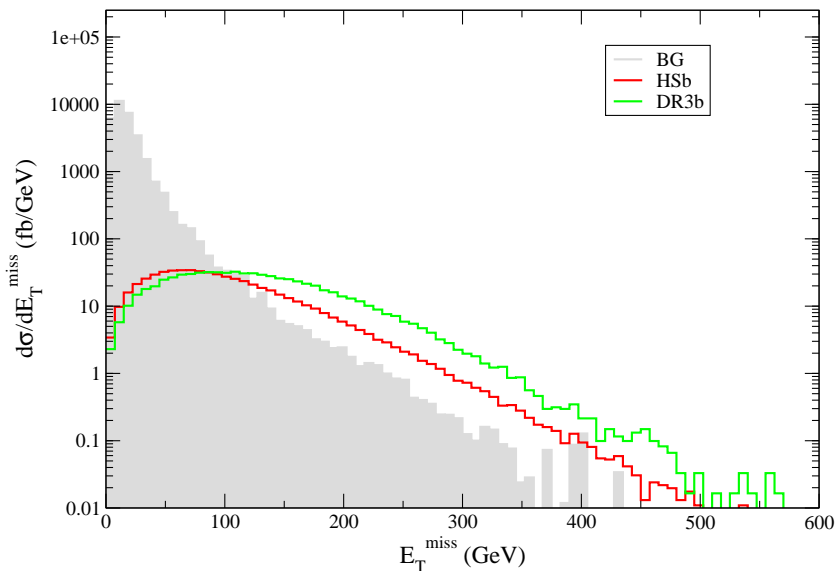


Figure 14: E_T^{miss} distribution for the BG (gray), HSb (red) and DR3b (green) points after the C0 cuts (see text).

- Lepton cuts: $E_T(\ell) \geq 10$ GeV and $\eta(\ell) \leq 2$,
- $S_T \geq 0.2$,
- $E_T^{\text{miss}} > 100$ GeV,

where $\ell = \mu, e$.

5.1 Multi b -jet + E_T^{miss} channel

The main effect of adding an E_T^{miss} cut to our previous analysis is the drastic reduction of background in the multi b -jet channel. However, the signal will also be significantly reduced, and so will be the statistics in the invariant mass distributions.

The $n(b)$ distribution after C1 cuts is shown in Fig. 15. Now the signal's peak at $n(b) = 1, 2$ is visible above the BG, and the hard distribution in $n(b)$ should be a striking signature for both the DR3b and HSb models, since the combined signal plus BG distribution becomes approximately flat for $0 \leq n(b) \leq 2$. The E_T^{miss} cut reduces most of the $b\bar{b}$ and $b\bar{b}b\bar{b}$ backgrounds, leaving $t\bar{t}$ as the dominant one for $n(b) \geq 1$. This results in a considerable reduction of the BG in the $n(b) = 1, 2$ and 3 bins, where now the signal/background ratio is larger than one. The cross-sections for $n(b) \geq 3, 4$ are shown in Table 4. Due to the large signal cross-section in these bins, the signal could be visible with less than 0.05 fb^{-1} of integrated luminosity (in the happy case where an E_T^{miss} measurement is immediately viable)!

The invariant mass distributions from Figs. 8 and 9 are now re-plotted in Figs. 16 and 17 after the E_T^{miss} cut is included. Now, due to the drastic reduction in the background, the $m_{b\bar{b}}$ distribution is nearly free of BG events. However, the decrease in the signal statistics

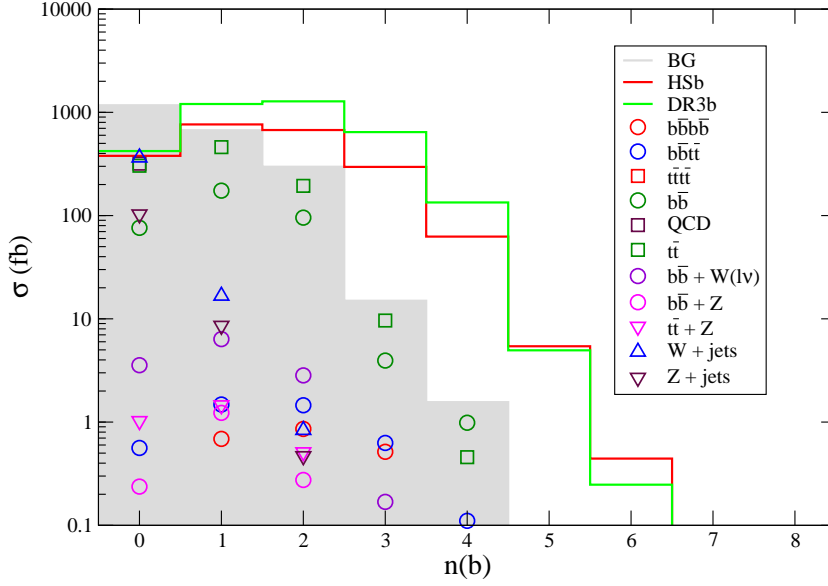


Figure 15: b -jet distribution after C1 cuts at the LHC, with $\sqrt{s} = 7$ TeV. We show the signal levels for the HSb (red) and DR3b (green) points along with various SM backgrounds.

Results after C1-based selection			
	$\sigma(n(b) \geq 3)$	$\sigma(n(b) \geq 4)$	$\sigma(\text{OS})$
HSb	364 fb	68 fb	81 fb
DR3b	782 fb	139 fb	23 fb
BG	16 fb	2 fb	9 fb

Table 4: Cross-sections for the $n(b) \geq 3, 4$ and OS channels after the C1 cuts for the points HSb, DR3b and the background.

makes it impossible to obtain any information on the sparticle masses from the shape of $\max[m_{b_1\bar{b}_1}, m_{b_2\bar{b}_2}]$.

A quantity that may still reveal some information on the gluino mass scale is the effective mass, $M_{\text{eff}} = \sum p_T(\text{jets}) + E_T^{\text{miss}}$, plotted in Fig. 18 for the HSb and DRb points, as well as for two points on the HS and DR3 model lines with heavier gluinos ($m_{\tilde{g}} = 576$ GeV and $m_{\tilde{g}} = 581$ GeV, respectively).

5.2 Multi-lepton channels

In Fig. 19, we show the isolated lepton multiplicity distribution after cuts C1. In the $n(\ell) = 0$ channel, the DR3b signal exceeds BG, while in the $n(\ell) = 2$ channel, the HSb signal exceeds BG. In the $n(\ell) = 1$ channel, BG from $t\bar{t}$ production is larger than both signal cases. One can pull out a better signal rate in the 1ℓ channel by imposing in addition a $M_T(\ell, E_T^{\text{miss}}) > 100$ GeV cut, as is well known [42].

We divide the $n(\ell) = 2$ channel into opposite-sign/same-flavor (OS/SF) events (e^+e^- or $\mu^+\mu^-$), and same-sign events. For the OS/SF channel, we see the E_T^{miss} cut has little effect on the signal-to-BG ratio, since the background, mainly $t\bar{t}$ production, also has large

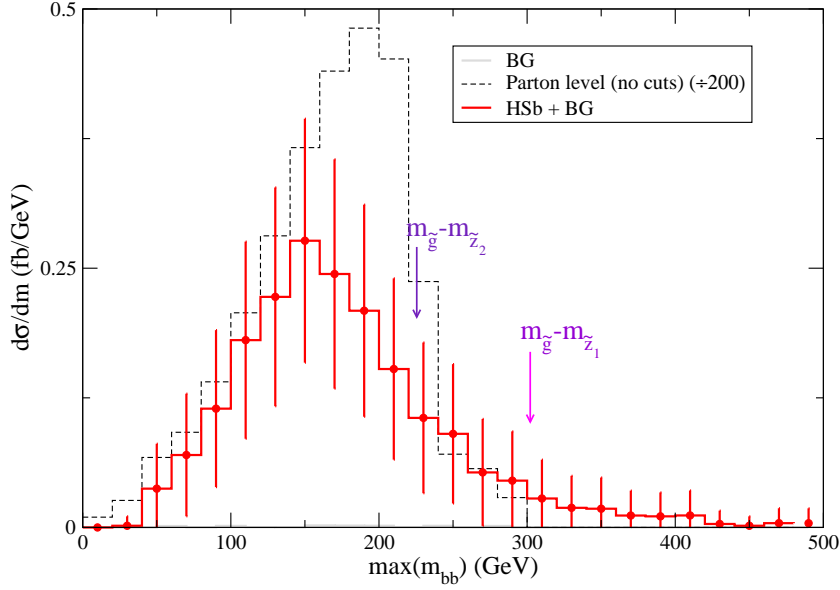


Figure 16: Same as Fig. 8, but including the $E_T^{\text{miss}} > 100$ GeV cut.

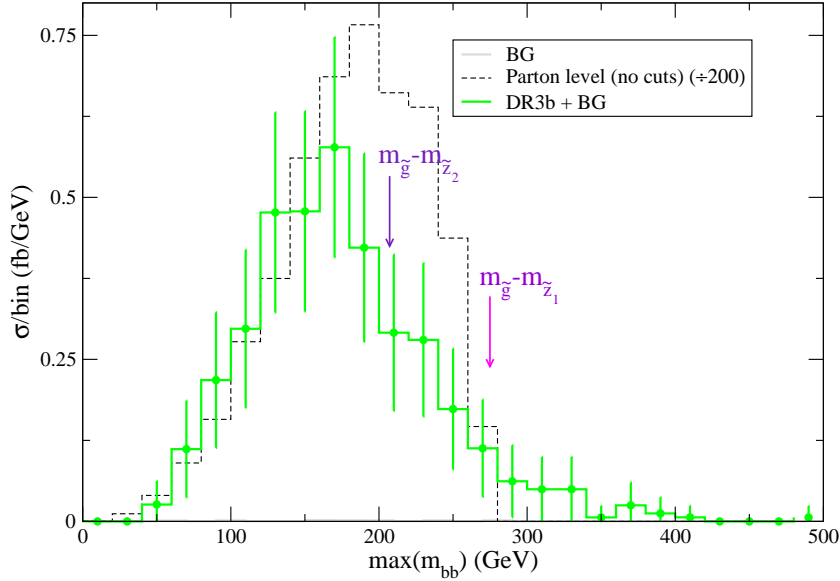


Figure 17: Same as Fig. 9, but including the $E_T^{\text{miss}} > 100$ GeV cut.

E_T^{miss} . Again, we expect the entire distribution to be self normalizing, since $t\bar{t}$ is the dominant BG, and one can fix the total $t\bar{t}$ cross section by normalizing to the 1ℓ channel. Then the $n(\ell)$ distribution should be harder than expected from just SM physics if a SUSY signal is present.

In Fig. 20, we show the OS/SF dilepton invariant mass distribution after cuts C1. Now, despite the negligible background, the reduction in the signal makes the mass edges less visible. In particular, the dilepton invariant mass still shows the $m_{\tilde{Z}_2} - m_{\tilde{Z}_1}$ edge, but with a smaller statistical significance as evident from the error bars. Performing a

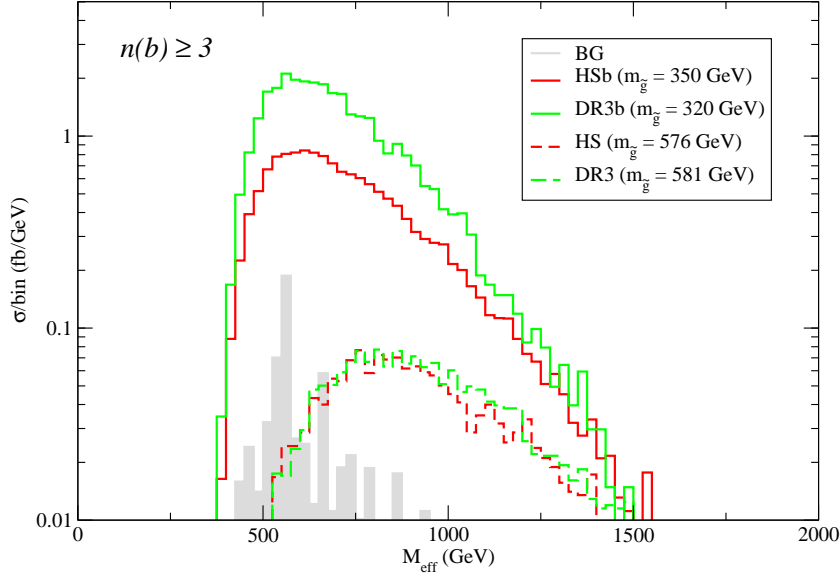


Figure 18: Effective mass scale of events with $n(b) \geq 3$ after C1 cuts for the BG, points HSb and DRb, and two points on the HS and DR3 model lines with heavier gluinos ($m_{\tilde{g}} = 576$ GeV and $m_{\tilde{g}} = 581$ GeV, respectively).

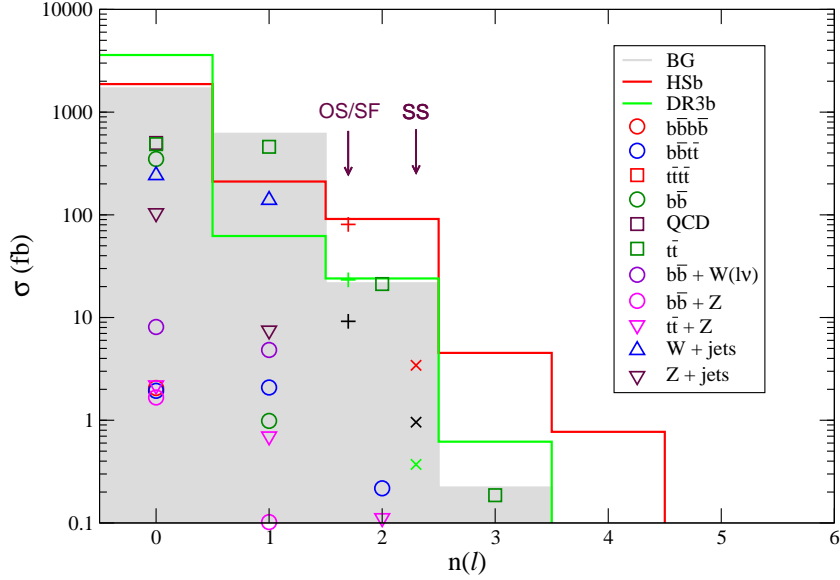


Figure 19: Lepton multiplicity distribution after C1 cuts at the LHC, with $\sqrt{s} = 7$ TeV. We show the signal levels for the HSb (red) and DR3b (green) points along with various SM backgrounds. In the $n(\ell) = 2$ bin, the left (pluses) and right (crosses) columns show the background (black) and signal components for OS/SF and SS dileptons.

different-flavor subtraction may reduce the already negligible BG even further.

5.3 Jets plus $Z \rightarrow \ell\bar{\ell} + E_T^{\text{miss}}$ signal

We also show in Fig. 20 two additional HS and DR3 cases with $m_{\tilde{g}} \sim 525$ GeV. In this case,

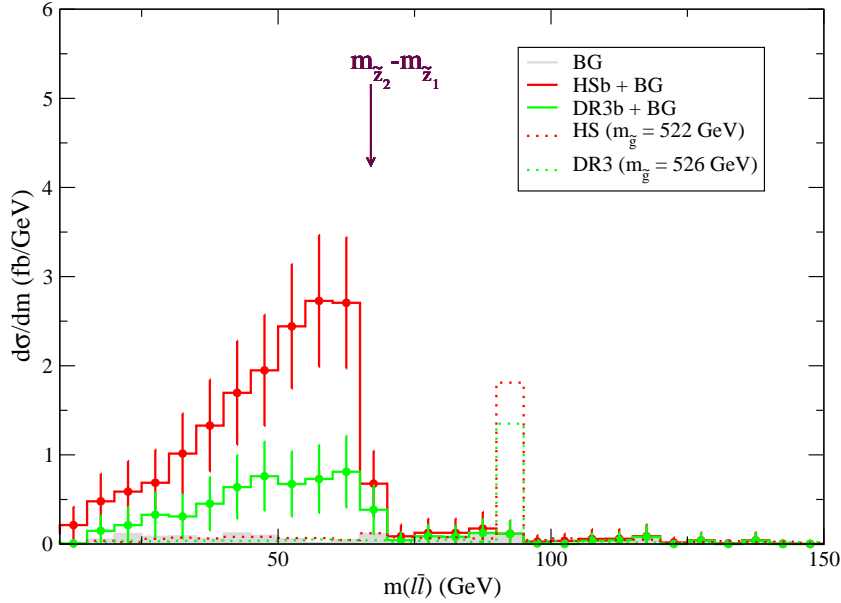


Figure 20: OS dilepton (μ 's and e 's) invariant mass for the HSb (red) and DR3b (green) points plus background events after the C1 cuts (see text). The BG distribution (gray) and the statistical error bars for 1 fb^{-1} of integrated luminosity are also shown.

according to Fig. 6, the value of $m_{\tilde{Z}_2}$ is high enough that the two-body decay $\tilde{Z}_2 \rightarrow \tilde{Z}_1 Z$ is now dominant. We then expect a signature of multiple b -jets plus E_T^{miss} plus a dilepton pair which reconstructs to $m(\ell^+ \ell^-) \simeq M_Z$ [43]. While signal rates can be very high for this channel, SM background is low, coming from processes such as $t\bar{t}$ and $Z + t\bar{t}$.

5.4 LHC reach for Yukawa-unified SUSY using E_T^{miss} and e ID

Next, we investigate the full LHC reach for Yukawa-unified SUSY along the HS and DR3 model lines. First, we require the cut set C1, which includes $E_T^{\text{miss}} > 100 \text{ GeV}$, and then require $n(b) \geq 2$ or $n(b) \geq 3$. The SM background level and 5σ level for 0.2 and 1 fb^{-1} are shown in the plots of Fig. 21, along with expected signal rates from the HS and DR3 model lines. For the $n(b) \geq 2$ case, we find an LHC reach for Yukawa-unified SUSY out to $m_{\tilde{g}} = 500$ (600) GeV for 0.2 (1) fb^{-1} . The reach is largely independent of whether one is in the HS or the DR3 model.

For $n(b) \geq 3$, the SM background is greatly reduced. In this case, we find a reach to $m_{\tilde{g}} = 540$ (630) GeV for 0.2 (1) fb^{-1} . Again, the reach in the multi- b -jet channel is largely independent of the model line, since both give large numbers of b -jets + E_T^{miss} in the final state. We have also calculated the reach in the $n(b) \geq 4$ channel; here, the result is qualitatively similar to that obtained in the $n(b) \geq 2$ case.

Next, in Fig. 22, we show the LHC reach for Yukawa-unified SUSY using the C1 cuts plus requiring a pair of OS/SF dileptons. In this case, the LHC reach is model dependent. For the HS model, where we obtain a high rate for $\tilde{g} \rightarrow b\bar{b}\tilde{Z}_2$ decays, we find a reach up to $m_{\tilde{g}} = 400$ (500) GeV for 0.2 (1) fb^{-1} of integrated luminosity. For the DR3 model line,

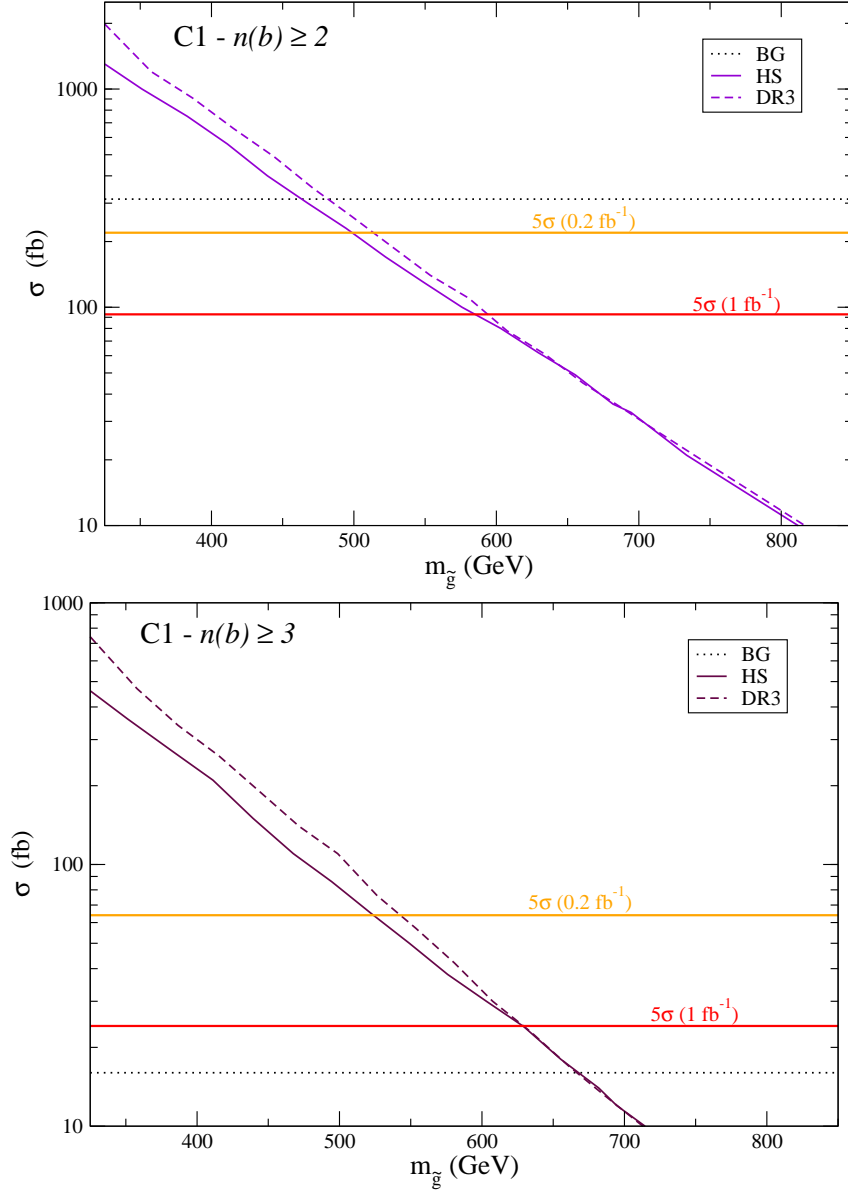


Figure 21: Early LHC reach for Yukawa-unified SUSY using cuts $C1$ plus $n_b \geq 2$ and $n_b \geq 3$.

there is no reach for 0.2 fb^{-1} , since here the $\tilde{g} \rightarrow b\bar{b}\tilde{Z}_1$ decay is dominant. With 1 fb^{-1} , however, a signal with 5σ significance should be visible for $m_{\tilde{g}} \sim 300 - 450 \text{ GeV}$.

For $m_{\tilde{g}} \gtrsim 450 \text{ GeV}$, the two body decay mode $\tilde{Z}_2 \rightarrow \tilde{Z}_1 Z$ opens up and we expect to reconstruct $Z \rightarrow e^+e^-$ and $Z \rightarrow \mu^+\mu^-$ within the class of signal events. Here, we will adopt cuts $C1$, but in addition require a OS/SF dilepton pair with $75 \text{ GeV} < m(\ell^+\ell^-) < 105 \text{ GeV}$ (cuts $C1'$). For this topology- ≥ 4 jets + $E_T^{\text{miss}} + Z \rightarrow \ell^+\ell^-$ - the dominant SM BG comes from $t\bar{t}$ production. The LHC reach is shown in Fig. 23. As can be seen, no significant excess is expected with 0.2 fb^{-1} of data. However, for $\gtrsim 1 \text{ fb}^{-1}$, we find that this topology can produce a 5σ signal for $m_{\tilde{g}} \sim 450 - 530 \text{ GeV}$ for both the HS and DR3

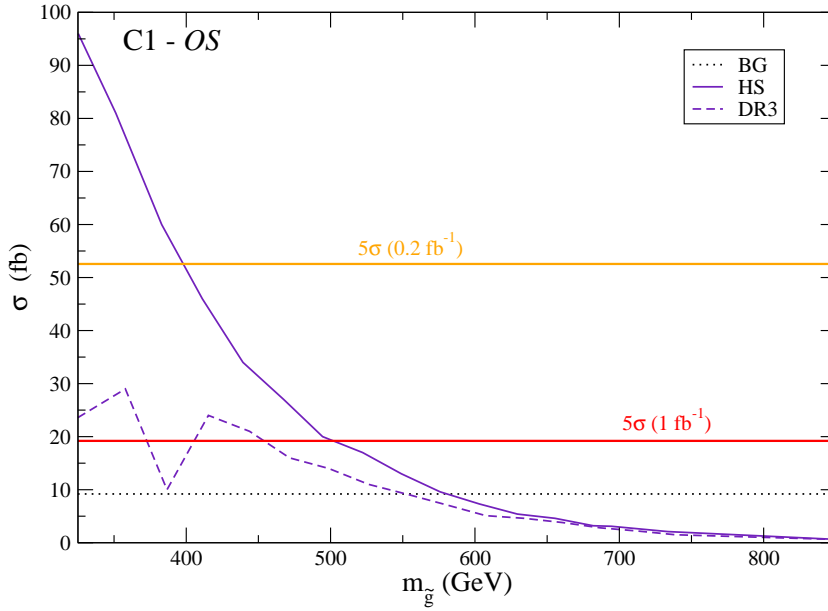


Figure 22: Early LHC reach for Yukawa-unified SUSY using cuts $C1$ for events containing OS/SF dileptons.

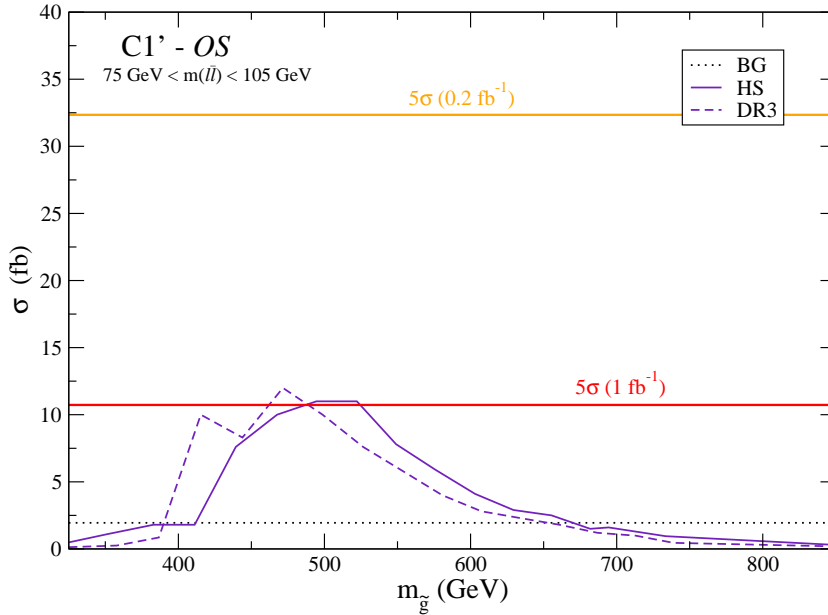


Figure 23: LHC reach for Yukawa-unified SUSY using cuts $C1'$ with a reconstructed leptonic Z boson.

model lines.

5.5 Differentiating the HS and DR3 models

Here we discuss the possibility of distinguishing the two models discussed so far using low luminosities and the channels investigated in the previous sections. As seen from last

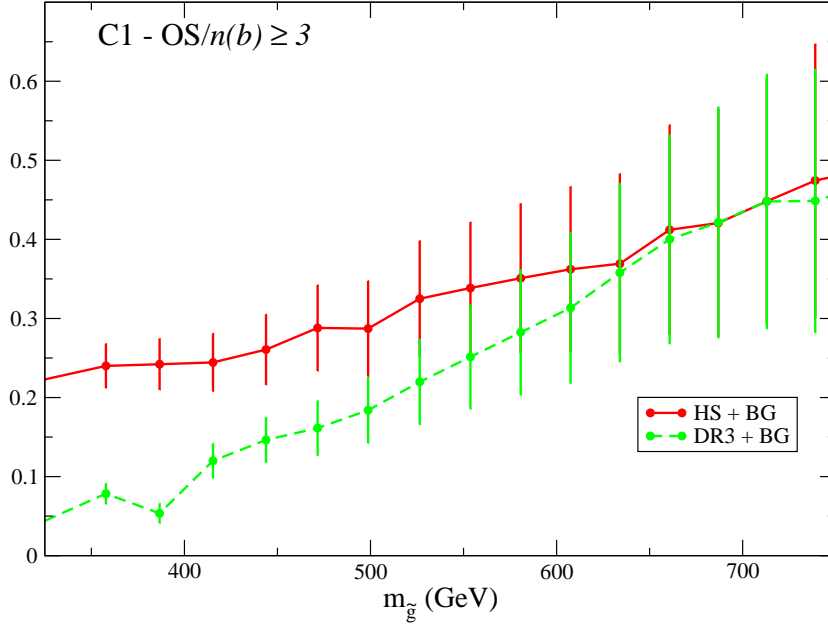


Figure 24: The ratio of the OS and $n(b) \geq 3$ cross-sections after C1 cuts for the HS and DR3 model lines plus background as a function of the gluino mass. We also show the statistical error bars for 1 fb^{-1} .

section results (Figs. 21 and 22) and the discussion in Sec. 2, for low to moderate $m_{\tilde{g}}$ masses we expect the HS and DR3 models to have rather distinct signatures. The first one is rich in multi- b jets ($n(b) \geq 4, 5$) and OS/SF dileptons coming from the $\tilde{g} \rightarrow \tilde{Z}_2 + b\bar{b}$ followed by $\tilde{Z}_2 \rightarrow Z/Z^* + b\bar{b}/\ell^+\ell^-$ decays, but has a softer E_T^{miss} spectrum due to the two step cascade decays. On the other hand, the DR3 model is mainly dominated by $\tilde{g} \rightarrow \tilde{Z}_1 + b\bar{b}$, with small cross-sections in the multi-lepton channels, a moderate number of b -jets ($n(b) \geq 3, 4$) and a harder E_T^{miss} spectrum. To explore these features and discuss how well we can distinguish both models with year one data, we plot in Fig. 24 the ratio of the OS and $n(b) \geq 3$ channels. As expected from the above discussion, we see that the ratio is larger for the HS model and suppressed in the DR3 case for $m_{\tilde{g}} \lesssim 600 \text{ GeV}$. As the gluino mass increases, the $\tilde{W}_1 + bt$ and $\tilde{Z}_1 + b\bar{b}$ gluino decay channels become available (see Fig. 5), increasing the OS channel in both models. From Fig. 24 we see that the OS/3b ratio should be a good discriminator up to $m_{\tilde{g}} \sim 450 \text{ GeV}$. For $m_{\tilde{g}} \gtrsim 450 \text{ GeV}$, higher luminosities are required in order to distinguish the models. But with high enough luminosities, we should be able to tell the models apart up to $m_{\tilde{g}} \sim 600 \text{ GeV}$. For even higher $m_{\tilde{g}}$ values, the signal features are too similar and the simple OS/3b ratio is no longer useful.

6. Comparison with CDF/CMS multijets + E_T^{miss} channel

Next we would like to compare our results for the multi- b -jets + E_T^{miss} signature with a multijets + E_T^{miss} analysis for SUSY searches proposed and used by CDF [44] and further developed in CMS [45]. We implement the following selection.

- $n(\text{jets}) \geq 3$ (we take jet $p_T > 50$ GeV),
- $E_T^{\text{miss}} \geq 150$ GeV,
- $\Delta\phi(\vec{E}_T^{\text{miss}}, \vec{H}_T) < 1$,
- $0.5 < R_2 \equiv \sqrt{\Delta\phi^2(j1, E_T^{\text{miss}}) + (\pi - \Delta\phi(j2, E_T^{\text{miss}}))^2} < 4$,
- $1.5 < R_{a1} \equiv \sqrt{(\Delta\phi(j2, E_T^{\text{miss}}))^2 + (\Delta\phi(j3, E_T^{\text{miss}}))^2} < 4.25$,
- $\Delta\phi(j2, E_T^{\text{miss}}) > 0.35$,
- $\Delta\phi(j_i, E_T^{\text{miss}}) > 0.3$,
- $|\eta(j1)| < 1.7$,
- Finally, we require the highest E_T object in each signal event to be hadronic, rather than leptonic ⁹.

The angular cuts are introduced in multijets + E_T^{miss} analyses where no lepton information is explicitly used in order to guarantee the discrimination of QCD backgrounds which may have large E_T^{miss} arising primarily due to jet mismeasurements. In such events, E_T^{miss} typically aligns with the 2nd hardest jet, as the hardest jet has a tendency to be mismeasured most and eventually becomes the 2nd hardest jet.

The reach results for CDF/CMS multijets + E_T^{miss} cuts with no $n(b)$ requirement can be seen in Fig. 25. The 5σ reach for 0.2 (1) fb^{-1} of integrated luminosity is found to be $m_{\tilde{g}} \sim 370$ (430) GeV.

In Figure 26, we plot the $n(b)$ signal and background distributions after CDF/CMS cuts, which share similar characteristics with the distributions after C1 cuts. The dominance of signal starting with $n(b) = 1$ illustrates the importance of considering b -jet tagging in the multijets + E_T^{miss} analyses. The original CMS analysis made use of the B -triggers to significantly enhance the signal/BG ratio, while here we directly cut on $n(b)$. We show in Table 5 the cross sections found after implementing CDF/CMS cuts with no requirement on $n(b)$ and with $n(b) = 1, 2, 3$.

⁹This is an approximation for the leading track isolation step of the indirect lepton veto (ILV) technique included in the CDF/CMS selection. Normally in multijets E_T^{miss} analyses where lepton information is not explicitly used, $W/Z/t\bar{t} + n$ jets backgrounds with leptonic W, Z decays can be eliminated by vetoing the events whose leading track is isolated. We omit the second step of ILV featuring jet electromagnetic and charged fractions since it is designed to eliminate machine and cosmic backgrounds which we do not consider here.

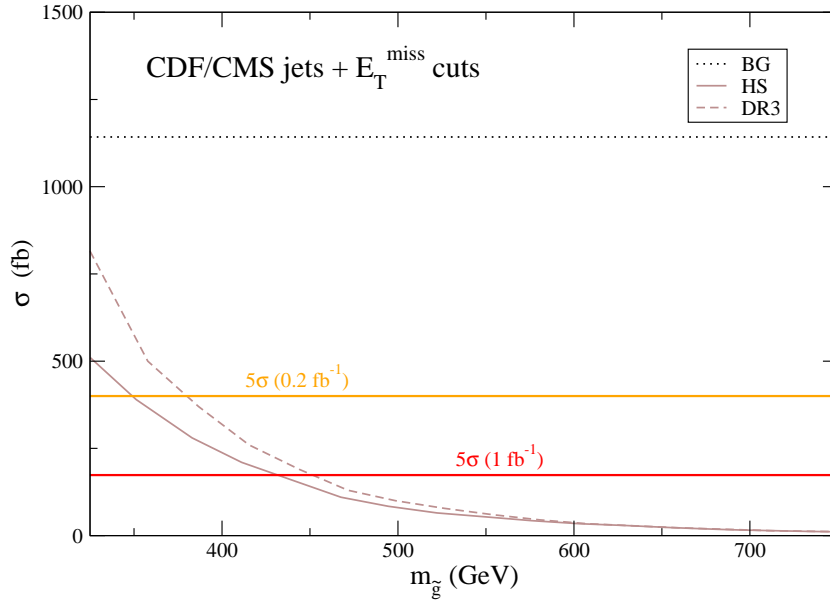


Figure 25: LHC reach for Yukawa-unified SUSY using CDF/CMS multijets + E_T^{miss} cuts with no $n(b)$ requirement.

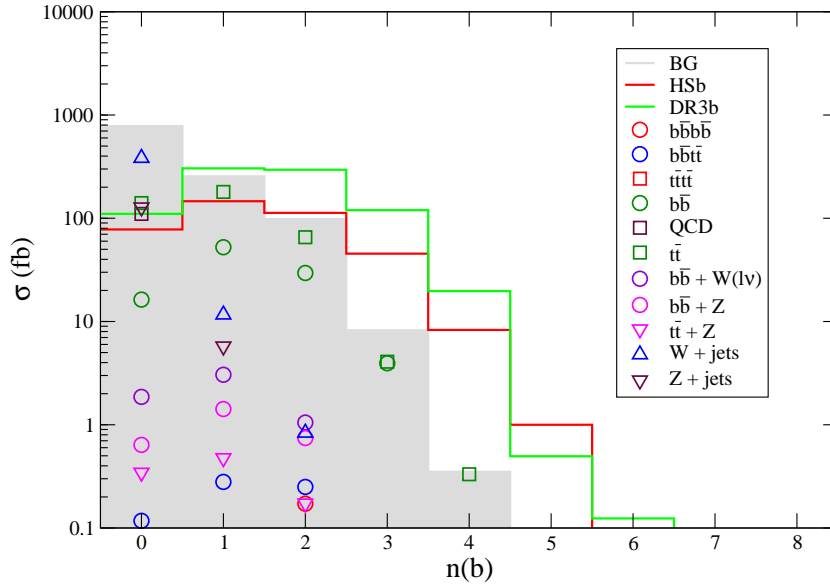


Figure 26: b -jet distribution after CDF/CMS multijets + E_T^{miss} cuts at the LHC, with $\sqrt{s} = 7$ TeV. We show the signal levels for the HSb (red) and DR3b (green) points along with various SM backgrounds.

As before, we can do much better by requiring a high multiplicity of b -jets. In Fig. 27, we adopt the same cuts as in Fig. 25, but in addition require $n(b) \geq 3$. In this case, the BG drops by a factor of ~ 150 , while the signal drops merely by a factor of ~ 7 for $m_{\tilde{g}} \sim 300$ GeV. The LHC reach increases to $m_{\tilde{g}} \sim 400$ (500) GeV for 0.2 (1) fb^{-1} of integrated luminosity.

Results after CDF/CMS multijets + E_T^{miss} -based selection				
	$\sigma(\text{no } n(b) \text{ req.})$	$\sigma(n(b) \geq 1)$	$\sigma(n(b) \geq 2)$	$\sigma(n(b) \geq 3)$
HSb	390 fb	313 fb	167 fb	55 fb
DR3b	849 fb	739 fb	435 fb	140 fb
BG	1132 fb	366 fb	101 fb	7 fb

Table 5: Cross-sections for the channels with no $n(b)$ requirement, $n(b) \geq 1$, 2 and 3 after the CDF/CMS multijets + E_T^{miss} cuts for the points HSb, DR3b and the background.

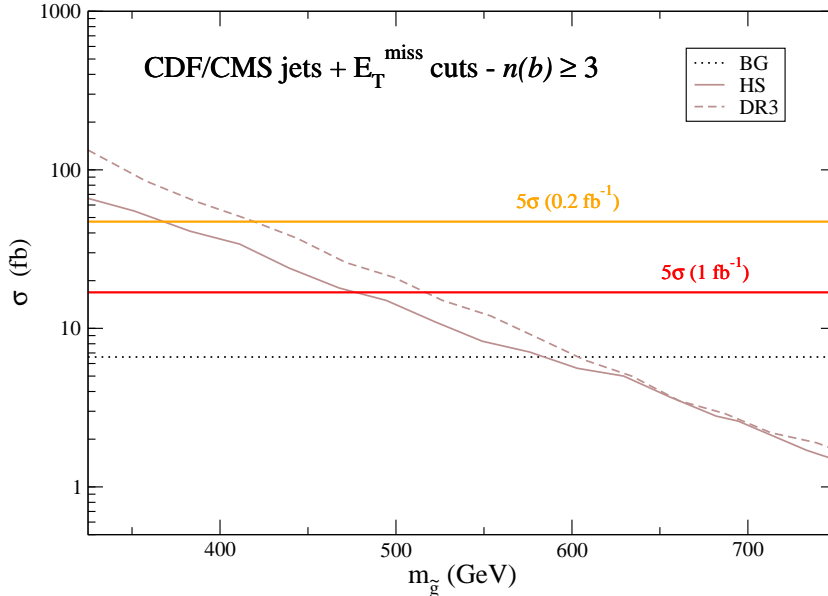


Figure 27: LHC reach for Yukawa-unified SUSY using CDF/CMS multijets + E_T^{miss} cuts with $n_b \geq 3$.

7. Conclusions

In $t-b-\tau$ Yukawa-unified SUSY, we expect a characteristic spectrum of superpartners with first/second generation squarks and sleptons around 10 TeV, third generation sparticles, heavy Higgs bosons and μ around the few TeV level, and very light gauginos, with $m_{\tilde{g}} \sim 300 - 500$ GeV (although here we consider even higher values). Thus, at LHC, we expect to see gluino pair production at a high rate, followed by gluino decays to $b\bar{b}\tilde{Z}_i$ or $t\bar{b}\tilde{W}_1^- + c.c.$ SUSY searches should therefore exploit the high multiplicity of b -jets expected in this scenario.

We investigated two model lines– the HS and DR3 cases. The HS case leads to large rates for OS/SF dileptons in the final state, while DR3 case does not. We computed numerous $2 \rightarrow 2$, $2 \rightarrow 3$ and $2 \rightarrow 4$ background processes. We found that with just $0.1-0.2 \text{ fb}^{-1}$ of integrated luminosity, the LHC discovery reach with $\sqrt{s} = 7$ TeV extends out to $m_{\tilde{g}} \sim 400$ GeV, even without using E_T^{miss} cuts. Crucial use is made of the high multiplicity of b -jets in the final state. In the case of the HS model, a corroborating signal appears in the $\mu^+\mu^- + jets + \geq 1$ b -jet channel.

	\mathcal{L} (fb $^{-1}$)	0.05	0.1	0.2	1
C0	HS	340 GeV	371 GeV	400 GeV	471 GeV
	<i>Channel</i>	$n(b) \geq 3$	$n(b) \geq 3$	$n(b) \geq 3$	$n(b) \geq 4$
	DR3	340 GeV	363 GeV	394 GeV	469 GeV
	<i>Channel</i>	$n(b) \geq 3$	$n(b) \geq 3$	$n(b) \geq 3$	$n(b) \geq 3$
C1	HS	436 GeV	480 GeV	526 GeV	630 GeV
	<i>Channel</i>	$n(b) \geq 3$	$n(b) \geq 3$	$n(b) \geq 3$	$n(b) \geq 3$
	DR3	460 GeV	506 GeV	545 GeV	630 GeV
	<i>Channel</i>	$n(b) \geq 3$	$n(b) \geq 3$	$n(b) \geq 3$	$n(b) \geq 3$
CDF/CMS	HS	-	341 GeV	380 GeV	474 GeV
	<i>Channel</i>	-	$n(b) \geq 1$	$n(b) \geq 1$	$n(b) \geq 3$
	DR3	350 GeV	382 GeV	420 GeV	516 GeV
	<i>Channel</i>	$n(b) \geq 2$	$n(b) \geq 2$	$n(b) \geq 2$	$n(b) \geq 3$

Table 6: Gluino 5σ mass reach for the HS and DR3 model lines for different luminosities. We show the values for the early search (C0 cuts), the full reach (C1 cuts) and the CDF/CMS multijets + E_T^{miss} cuts (CDF/CMS). We also show the channel which optimizes the reach.

The LHC reach at very low luminosity and without E_T^{miss} is comparable to the Tevatron reach in the multi- b + E_T^{miss} channel with 5–10 fb $^{-1}$ of data. This may lead to a tight competition for the discovery or exclusion of the simplest Yukawa-unified SUSY scenario!

Moving beyond about 0.2 fb $^{-1}$, we expect reliable E_T^{miss} resolution and electron identification to become available. We find that the LHC reach, using $\sqrt{s} = 7$ TeV and 1 fb $^{-1}$ of integrated luminosity, will move into the $m_{\tilde{g}} \sim 600 - 650$ GeV range for both the HS and DR3 model lines, if we require $E_T^{\text{miss}} \geq 100$ GeV along with $n(b) \geq 3$. This reach is presumably sufficient to rule out Yukawa unification in the DR3 case. In the HS case, somewhat larger values of $m_{\tilde{g}}$ can be allowed, although they seem very improbable. The LHC reach for 1 fb $^{-1}$ using the multi-jets + E_T^{miss} signature– but making no requirement on $n(b)$ – turns out to be much lower. A summary of our various results is presented in a convenient form in Table 6.

At some point LHC energy will be increased to ~ 10 TeV, and this will allow the reach to be extended past the values presented here. Thus, our main conclusion is that LHC stands an excellent chance to either discover Yukawa-unified SUSY during year 1 of operation, or exclude almost all its model parameter space!

Last but not least we note that, if the scenario discussed here is realized, a trilepton signal from Drell-Yang $\widetilde{W}_1 \widetilde{Z}_2$ production should appear when moving into the several fb $^{-1}$ regime, giving direct access to the chargino/neutralino sector.

Note added: While finalizing this manuscript, we found an Atlas note [46] which also investigates using multiple b -jets to enhance the LHC reach for SUSY in the mSUGRA model. They examine integrated luminosity values of 0.1 and 1 fb $^{-1}$, but take $\sqrt{s} = 14$ TeV. Their overall results seem quite consistent with the results given here.

Acknowledgments

We thank Harrison Prosper for sharing with us his p-value and significance code. This research was supported in part by the U.S. Department of Energy grant number DE-FG-97ER41022, by the Fulbright Program and CAPES (Brazilian Federal Agency for Post-Graduate Education). The work of SK is supported in part by the French ANR project ToolsDMColl, BLAN07-2-194882.

References

- [1] For recent reviews, see R. Mohapatra, hep-ph/9911272 (1999) and S. Raby, in Rept. Prog. Phys. **67** (2004) 755.
- [2] H. Georgi, in *Proceedings of the American Institute of Physics*, edited by C. Carlson (1974); H. Fritzsch and P. Minkowski, Ann. Phys. **93**, 193 (1975); M. Gell-Mann, P. Ramond and R. Slansky, Rev. Mod. Phys. **50**, 721 (1978).
- [3] P. Minkowski, *Phys. Lett.* **B 67** (1977) 421; M. Gell-Mann, P. Ramond and R. Slansky, in *Supergravity, Proceedings of the Workshop*, Stony Brook, NY 1979 (North-Holland, Amsterdam); T. Yanagida, KEK Report No. 79-18, 1979; R. Mohapatra and G. Senjanovic, *Phys. Rev. Lett.* **44** (1980) 912.
- [4] B. Ananthanarayan, G. Lazarides and Q. Shafi, *Phys. Rev.* **D 44** (1991) 1613 and *Phys. Lett.* **B 300** (1993) 245; G. Anderson *et al.* *Phys. Rev.* **D 47** (1993) 3702 and *Phys. Rev.* **D 49** (1994) 3660; V. Barger, M. Berger and P. Ohmann, *Phys. Rev.* **D 49** (1994) 4908; M. Carena, M. Olechowski, S. Pokorski and C. Wagner, Ref. [17]; B. Ananthanarayan, Q. Shafi and X. Wang, *Phys. Rev.* **D 50** (1994) 5980; R. Rattazzi and U. Sarid, *Phys. Rev.* **D 53** (1996) 1553; T. Blazek, M. Carena, S. Raby and C. Wagner, *Phys. Rev.* **D 56** (1997) 6919; T. Blazek and S. Raby, *Phys. Lett.* **B 392** (1997) 371; T. Blazek and S. Raby, *Phys. Rev.* **D 59** (1999) 095002; T. Blazek, S. Raby and K. Tobe, *Phys. Rev.* **D 60** (1999) 113001 and *Phys. Rev.* **D 62** (2000) 055001; see also [5].
- [5] S. Profumo, *Phys. Rev.* **D 68** (2003) 015006; C. Pallis, *Nucl. Phys.* **B 678** (2004) 398; M. Gomez, G. Lazarides and C. Pallis, *Phys. Rev.* **D 61** (2000) 123512, *Nucl. Phys.* **B 638** (2002) 165 and *Phys. Rev.* **D 67** (2003) 097701; U. Chattopadhyay, A. Corsetti and P. Nath, *Phys. Rev.* **D 66** (2002) 035003; M. Gomez, T. Ibrahim, P. Nath and S. Skadhauge, *Phys. Rev.* **D 72** (2005) 095008.
- [6] H. Baer, M. Diaz, J. Ferrandis and X. Tata, *Phys. Rev.* **D 61** (2000) 111701; H. Baer, M. Brhlik, M. Diaz, J. Ferrandis, P. Mercadante, P. Quintana and X. Tata, *Phys. Rev.* **D 63** (2001) 015007.
- [7] H. Baer and J. Ferrandis, *Phys. Rev. Lett.* **87** (2001) 211803;
- [8] T. Blazek, R. Dermisek and S. Raby, *Phys. Rev. Lett.* **88** (2002) 111804; T. Blazek, R. Dermisek and S. Raby, *Phys. Rev.* **D 65** (2002) 115004; R. Dermisek, S. Raby, L. Roszkowski and R. Ruiz de Austri, *J. High Energy Phys.* **0304** (2003) 037; R. Dermisek, S. Raby, L. Roszkowski and R. Ruiz de Austri, *J. High Energy Phys.* **0509** (2005) 029.
- [9] D. Auto, H. Baer, C. Balazs, A. Belyaev, J. Ferrandis and X. Tata, *J. High Energy Phys.* **0306** (2003) 023.
- [10] C. Balazs and R. Dermisek, *J. High Energy Phys.* **0803** (2003) 024.

- [11] H. Baer, S. Kraml, S. Sekmen and H. Summy, *J. High Energy Phys.* **0803** (2008) 056.
- [12] W. Altmannshofer, D. Guadagnoli, S. Raby and D. Straub, *Phys. Lett.* **B 668** (2008) 385.
- [13] I. Gogoladze, R. Khalid and Q. Shafi, *Phys. Rev.* **D 79** (2009) 115004.
- [14] D. Guadagnoli, S. Raby and D. M. Straub, *J. High Energy Phys.* **0910** (2009) 059.
- [15] H. Baer, S. Kraml and S. Sekmen, *J. High Energy Phys.* **0909** (2009) 005.
- [16] S. P. Martin and M. Vaughn, *Phys. Rev.* **D 50** (1994) 2282.
- [17] R. Hempfling, *Phys. Rev.* **D 49** (1994) 6168; L. J. Hall, R. Rattazzi and U. Sarid, *Phys. Rev.* **D 50** (1994) 7048; M. Carena *et al.*, *Nucl. Phys.* **B 426** (1994) 269; D. Pierce, J. Bagger, K. Matchev and R. Zhang, *Nucl. Phys.* **B 491** (1997) 3.
- [18] J. Feng, C. Kolda and N. Polonsky, *Nucl. Phys.* **B 546** (1999) 3; J. Bagger, J. Feng and N. Polonsky, *Nucl. Phys.* **B 563** (1999) 3; J. Bagger, J. Feng, N. Polonsky and R. Zhang, *Phys. Lett.* **B 473** (2000) 264. H. Baer, P. Mercadante and X. Tata, *Phys. Lett.* **B 475** (2000) 289; H. Baer, C. Balazs, M. Brhlik, P. Mercadante, X. Tata and Y. Wang, *Phys. Rev.* **D 64** (2001) 015002.
- [19] H. Murayama, M. Olechowski and S. Pokorski, *Phys. Lett.* **B 371** (1996) 57.
- [20] R. Peccei and H. Quinn, *Phys. Rev. Lett.* **38** (1977) 1440 and *Phys. Rev.* **D 16** (1977) 1791.
- [21] S. Weinberg, *Phys. Rev. Lett.* **40** (1978) 223; F. Wilczek, *Phys. Rev. Lett.* **40** (1978) 279.
- [22] J. E. Kim, *Phys. Rev. Lett.* **43** (1979) 103; M. A. Shifman, A. Vainstein and V. I. Zakharov, *Nucl. Phys.* **B 166** (1980) 493.
- [23] M. Dine, W. Fischler and M. Srednicki, *Phys. Lett.* **B 104** (1981) 199; A. P. Zhitnitskii, *Sov. J. Nucl.* **31** (1980) 260.
- [24] For recent reviews on axion physics, see J. E. Kim and G. Carosi, arXiv:0807.3125 (2008); P. Sikivie, hep-ph/0509198; M. Turner, *Phys. Rept.* **197** (1990) 67.
- [25] H. P. Nilles and S. Raby, *Nucl. Phys.* **B 198** (1982) 102; J. E. Kim and H. P. Nilles, *Phys. Lett.* **B 138** (1984) 150; J. E. Kim, *Phys. Lett.* **B 136** (1984) 378.
- [26] G. Lazarides and Q. Shafi, *Phys. Lett.* **B 258** (1991) 305; K. Kumekawa, T. Moroi and T. Yanagida, *Prog. Theor. Phys.* **92** (1994) 437; T. Asaka, K. Hamaguchi, M. Kawasaki and T. Yanagida, *Phys. Lett.* **B 464** (1999) 12.
- [27] H. Murayama and T. Yanagida, *Phys. Lett.* **B 322** (1994) 349; M. Dine, L. Randall and S. Thomas, *Nucl. Phys.* **B 458** (1996) 291.
- [28] H. Baer, M. Haider, S. Kraml, S. Sekmen and H. Summy, JCAP**0902** (2009) 002.
- [29] H. Baer, S. Kraml, S. Sekmen and H. Summy, arXiv:0910.2988 (2009).
- [30] H. Baer, S. Kraml, S. Sekmen and H. Summy, *J. High Energy Phys.* **0810** (2008) 079.
- [31] F. Gianotti and M. Mangano, hep-ph/0505221; D. Green, hep-ph/0601038; H. Baer, V. Barger and G. Shaughnessy, *Phys. Rev.* **D 78** (2008) 095009; J. Hubisz, J. Lykken, M. Pierini and M. Spiropulu, *Phys. Rev.* **D 78** (2008) 075008; M. Mangano, *Eur. Phys. J.* **C 59** (2009) 373.
- [32] H. Baer, H. Prosper and H. Summy, *Phys. Rev.* **D 77** (2008) 055017; H. Baer, A. Lessa and H. Summy, *Phys. Lett.* **B 674** (2009) 49; J. Edsjo, E. Lundstrom, S. Rydbeck and J. Sjolín, arXiv:0910.1106 (2009).

- [33] H. Baer, V. Barger, A. Lessa and X. Tata, *J. High Energy Phys.* **0909** (2009) 063.
- [34] W. Beenakker, R. Hopker, M. Spira, [hep-ph/9611232](#) (1996).
- [35] U. Chattopadhyay, A. Datta, A. Datta, A. Datta and D.P. Roy, *Phys. Lett.* **B 493** (2000) 127; P. Mercadante, K. Mizukohi and X. Tata, *Phys. Rev.* **D 72** (30005) 035009; S. P. Das et al. *Eur. Phys. J.* **C 54** (2008) 645; R. Kadala et al. *Eur. Phys. J.* **C 56** (2008) 511
- [36] H. Baer, C. H. Chen, M. Drees, F. Paige and X. Tata, *Phys. Rev. Lett.* **79** (1997) 986 and *Phys. Rev.* **D 58** (1998) 075008.
- [37] M. Mangano, M. Moretti, F. Piccinini, R. Pittau and A. Polosa, *J. High Energy Phys.* **0307** (2003) 001.
- [38] T. Stelzer and W. F. Long, *Comput. Phys. Commun.* **81** (1994) 357.
- [39] T. Sjostrand, S. Mrenna and P. Skands, *J. High Energy Phys.* **0605** (2006) 026.
- [40] ISAJET v7.79, by H. Baer, F. Paige, S. Protopopescu and X. Tata, [hep-ph/0312045](#); for details on the Isajet spectrum calculation, see H. Baer, J. Ferrandis, S. Kraml and W. Porod, *Phys. Rev.* **D 73** (2006) 015010.
- [41] H. B. Prosper, private code for calculation of significance from p-values.
- [42] H. Baer, C. H. Chen, F. Paige and X. Tata, *Phys. Rev.* **D 53** (1996) 6241.
- [43] H. Baer, X. Tata and J. Woodside, *Phys. Rev.* **D 42** (1990) 1450; H. Baer, C. Balazs, A. Belyaev, T. Krupovnickas and X. Tata, *J. High Energy Phys.* **0306** (2003) 054.
- [44] M. Spiropulu, Ph. D. thesis, UMI-99-88600; A. A. Affolder et al. (CDF Collaboration), *Phys. Rev. Lett.* **88** (2002) 041801 [hep-ex/0106001](#); S. Sekmen, Ph. D. thesis, CMS TS-2009/025
- [45] S. Sekmen, Ph. D. thesis, CMS TS-2009/025
- [46] *Discovery potential for supersymmetry with b-jet final states with the Atlas detector*, (The Atlas Collaboration), Atlas note ATL-PHYS-PUB-2009-075 (2009).